Quantifying the shape of cells - from Minkowski tensors to p-atic order

Lea Happel[1†], Griseldis Oberschelp[1†], Valeriia Grudtsyna[2], Harish P. Jain[3], Rastko Sknepnek[4,5], Amin Doostmohammadi[2], Axel Voigt[1,6,7*]

***For correspondence:** axel.voigt@tu-dresden.de (AV)

[†]These authors contributed equally to this work

[1]Institute of Scientific Computing, TU Dresden, 01062 Dresden, Germany; [2]Niels Bohr Institute, University of Copenhagen, Kobenhavn, 2100, Denmark; [3]Njord Centre, Physics Department, University of Oslo, Oslo, Norway; [4]School of Life Sciences, University of Dundee, Dundee DD1 5EH, United Kingdom; [5]School of Science and Engineering, University of Dundee, Dundee DD1 4HN, United Kingdom; [6]Center of Systems Biology Dresden, Pfotenhauerstr. 108, 01307 Dresden, Germany; [7]Cluster of Excellence, Physics of Life, TU Dresden, Arnoldstr. 18, 01307 Dresden, Germany

Abstract P-atic liquid crystal theories offer new perspectives on how cells self-organize and respond to mechanical cues. Understanding and quantifying the underlying orientational orders is therefore essential for unraveling the physical mechanisms that govern tissue dynamics. Due to the deformability of cells this requires quantifying their shape. We introduce rigorous mathematical tools and a reliable framework for such shape analysis. Applying this to segmented cells in MDCK monolayers and computational approaches for active vertex models and multiphase field models challenges previous findings and opens new pathways for understanding the role of orientational symmetries and p-atic liquid crystal theories in tissue mechanics and development.

Introduction

The importance of orientational order in biological systems is becoming increasingly clear, as it plays a critical role in processes such as tissue morphogenesis, collective cell motion, and cellular extrusion. Orientational order results from the shapes of cells and their alignments with neighboring cells. Disruptions in this order, known as topological defects, are often linked to key biological events. For instance, defects—points or lines where the order breaks down—can drive cell extrusion (***Saw et al., 2017***; ***Monfared et al., 2023***) or trigger morphological changes in tissues (***Maroudas-Sacks et al., 2021***; ***Ravichandran et al., 2024***). Orientational order is linked to liquid crystal theories and should here be interpreted in a broad sense. Recent evidence extends beyond nematic order, characterized by symmetry under $180° = 2\pi/2$ rotation, to higher-order symmetries such as tetratic order ($90° = 2\pi/4$), hexatic order ($60° = 2\pi/6$), and even general p-atic orders ($2\pi/p$, p being an integer). In biological contexts, nematic order ($p = 2$) has been widely studied in epithelial tissues (***Duclos et al., 2017***; ***Saw et al., 2017***; ***Kawaguchi et al., 2017***), linking defects to cellular behaviors and tissue organization. More complex orders, such as tetratic order ($p = 4$) (***Cislo et al., 2023***) and hexatic oder ($p = 6$) (***Li and Ciamarra, 2018***; ***Durand and Heu, 2019***; ***Pasupalak et al., 2020***; ***Armengol-Collado et al., 2023***; ***Eckert et al., 2023***), have also been observed in experimental systems, offering new perspectives on how cells self-organize and respond to mechanical cues. Understanding and quantifying orientational order and the corresponding liquid crystal theory are therefore essential for unraveling the physical mechanisms that govern biological dynamics.

In physics, p-atic liquid crystals illustrate how particle shape and symmetry influence phase behavior, with seminal works dating back to Onsager's theories (***Onsager, 1949***). Most prominently, hexatic order ($p = 6$) has been postulated and found by experiments and simulations as an intermediate state between crystalline solid and isotropic liquid in (***Halperin and Nelson, 1978***; ***Nelson and Halperin, 1979***; ***Murray and Van Winkle, 1987***; ***Bladon and Frenkel, 1995***; ***Zahn et al., 1999***; ***Gasser et al., 2010***; ***Bernard and Krauth, 2011***). Other examples are colloidal systems for triadic platelets (***Bowick et al., 2017***) or cubes (***Wojciechowski and Frenkel, 2004***), which lead to p-atic order with $p = 3$ and $p = 4$, respectively. Even pentatic ($p = 5$) and heptatic ($p = 7$) liquid crystals have been engineered (***Wang and Mason, 2018***; ***Yu and Mason, 2023***). The corresponding liquid crystal theories for p-atic order have only recently been defined (***Giomi et al., 2022***; ***Krommydas et al., 2023***) and can also be used in biological contexts. However, while in colloidal systems particle shapes remain fixed, in biological tissues, cells are dynamic: their shapes are irregular, variable, and influenced by internal and external forces. These unique properties make quantifying p-atic order in tissues significantly more challenging, as quantification of the cell shapes is required. We will demonstrate that existing methods, such as bond-orientational order (***Nelson and Halperin, 1979***) or polygonal shape analysis (***Armengol-Collado et al., 2023***), often fail to capture the nuances of irregular cell shapes, which has severe consequences on the definition of p-atic order.

To address this, we adapt Minkowski tensors (***Mecke, 2000***; ***Schröder-Turk et al., 2013***)—rigorous mathematical tools for shape analysis—to quantify p-atic order in cell monolayers. Minkowski tensors provide robust and sensitive measures of shape anisotropy and orientation, accommodating both smooth and polygonal shapes while remaining resilient to small perturbations. By applying these tools, we re-examine previous conclusions about p-atic order in epithelial tissues and demonstrate that certain widely accepted results require reconsideration.

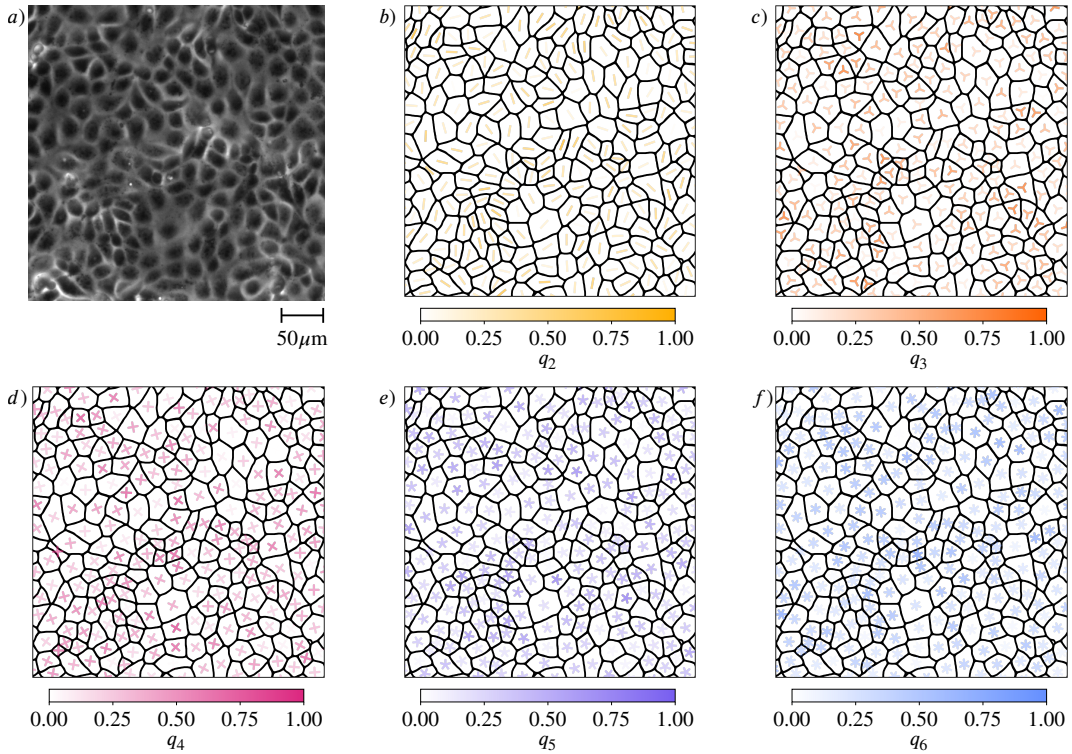

Figure 1. Shape classification of cells in wild-type MDCK cell monolayer. a) Raw experimental data. b) - f) Minkowski tensor, visualized using ϑ_p and q_p, ***Equation 7*** (see Methods and materials) for $p = 2, 3, 4, 5, 6$, respectively. The brightness and the rotation of the p-atic director indicates the magnitude and the orientation, respectively.

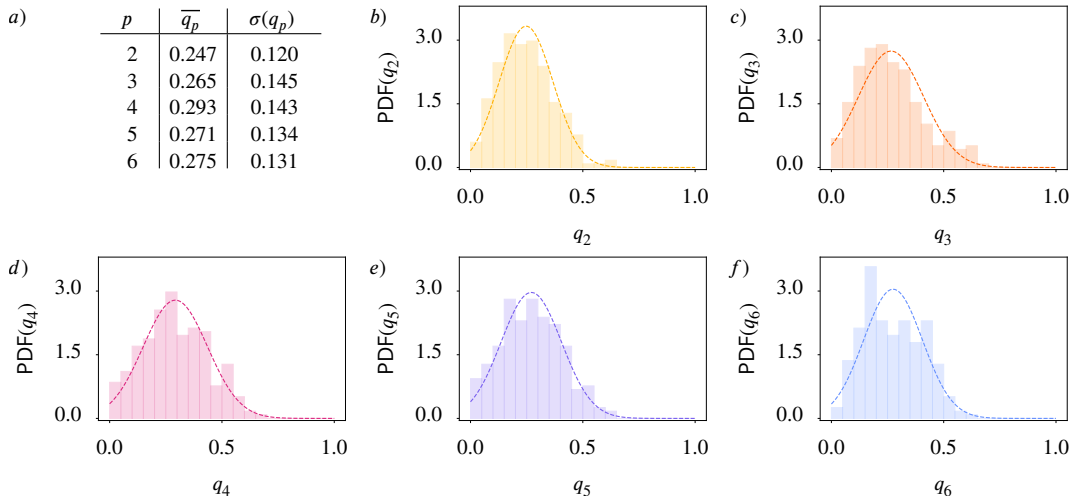

p	$\overline{q_p}$	$\sigma(q_p)$
2	0.247	0.120
3	0.265	0.145
4	0.293	0.143
5	0.271	0.134
6	0.275	0.131

Figure 2. Statistical data for cell shapes identified in ***Figure 1*** (see Methods and materials). a) Mean $\overline{q_p}$ and standard deviation $\sigma(q_p)$ of q_p. b) - f) Probability distribution function (PDF) of q_p for $p = 2, 3, 4, 5, 6$, respectively. Normal distributions with the same mean and standard deviations are added to the histograms as a guide to the eye.

Our study leverages a combination of experimental and computational approaches. Experimentally, we analyze confluent monolayers of MDCK (Madin-Darby Canine Kidney) cells, comparing wild-type tissues with E-cadherin knockout variants to explore the role of cell-cell adhesion in orientational order. ***Figure 1*** provide a snapshot of the considered monolayer of wild-type MDCK cells, together with their shape classification by Minkowski tensors. The corresponding statistical data and probability distributions of these quantities are shown in ***Figure 2***. These data already indicate no clear preference of a specific p-atic order and the necessity for robust and sensitive shape classification. Computationally, we employ two complementary models for cell monolayers: the active vertex model and the multiphase field model. These approaches allow us to systematically vary parameters such as cell activity and mechanical properties, providing a comprehensive view of how p-atic order emerges in different contexts.

By combining these robust mathematical tools, experimental insights, and computational models, we establish a reliable framework for quantifying p-atic order in biological tissues. This framework not only challenges previous findings but also opens new pathways for understanding the role of orientational symmetries in tissue mechanics and development.

Methods and materials

Minkowski tensors

Essential properties of the geometry of a two-dimensional object are summarized by scalar-valued size measures, so called Minkowski functionals. They are defined by

$$W_0(\mathcal{C}) = \int_{\mathcal{C}} \mathrm{d}\mathcal{C}, \quad W_1(\mathcal{C}) = \int_{\partial\mathcal{C}} \mathrm{d}\partial\mathcal{C}, \text{ and } \quad W_2(\mathcal{C}) = \int_{\partial\mathcal{C}} \mathcal{H}\, \mathrm{d}\partial\mathcal{C}, \tag{1}$$

where $\mathcal{C}$ is the smooth two-dimensional object, with contour $\partial\mathcal{C}$ and $\mathcal{H}$ denotes the curvature of the contour $\partial\mathcal{C}$ (see ***Figure 3*** for a schematic description), as reviewed in ***Mecke*** (***2000***). They describe (up to field-specific prefactors) the area, the perimeter and a curvature-weighted integral of the contour, respectively. Minkowski functionals are also known as intrinsic volumes. For convex objects, they have been shown to be continuous and invariant to translations and rotations. Due to these properties and Hadwiger's characterization theorem (***Hadwiger, 1975***), they are natural size descriptors that provide essential and complete information about invariant geometric features. However, these properties also set limits to their use as shape descriptors. Due to rotation

invariance, they are unable to capture the orientation of the shape. To describe more complex shape information the scalar-valued Minkowski functionals are extended to a set of tensor-valued descriptors, known as Minkowski tensors. These objects have been investigated both in mathematical (***Alesker, 1999***; ***Hug et al., 2008***, ***2007***; ***McMullen, 1997***) and in physical literature (***Schröder-Turk et al., 2010a***; ***Kapfer et al., 2012***). Using tensor products of the position vectors $\mathbf{r}$ and the normal vectors $\mathbf{n}$ of the contour $\partial\mathcal{C}$, defined as $\mathbf{r}^a \odot \mathbf{n}^b = \mathbf{r} \odot \ldots \odot \mathbf{r} \odot \mathbf{n} \odot \ldots \odot \mathbf{n}$, the first considered a times and the last b times with $\odot$ denoting the symmetrized tensor product. The Minkowski tensors are defined as

$$\mathbf{W}_0^{a,0}(\mathcal{C}) = \int_{\mathcal{C}} \mathbf{r}^a \,\mathrm{d}\mathcal{C}, \quad \mathbf{W}_1^{a,b}(\mathcal{C}) = \int_{\partial\mathcal{C}} \mathbf{r}^a \odot \mathbf{n}^b \,\mathrm{d}\partial\mathcal{C}, \text{ and } \quad \mathbf{W}_2^{a,b}(\mathcal{C}) = \int_{\partial\mathcal{C}} \mathbf{r}^a \odot \mathbf{n}^b \mathcal{H} \,\mathrm{d}\partial\mathcal{C}. \tag{2}$$

For $\mathbf{W}_j^{0,0}(\mathcal{C}) = W_j(\mathcal{C})$ for $j = 0, 1, 2$, so the Minkowski tensors are extensions of the Minkowski functionals. In analogy to Minkowski functionals also Minkowski tensors have been shown to be continuous for convex objects. Also, analogies to Hadwiger's characterization theorem exist (***Alesker, 1999***). However, for our purpose, the essential property is the continuity. It makes Minkowski functionals and Minkowski tensors a robust measure as small shape changes lead to small changes in the shape descriptor. Due to this property, Minkowski tensors have been successfully used as shape descriptors in different fields, e.g. in materials science as a robust measure of anisotropy in porous (***Schröder-Turk et al., 2010b***) and granular material (***Schröder-Turk et al., 2013***), in astrophysics to describe morphology of galaxies (***Beisbart et al., 2002***), and in biology to distinguish shapes of different types of neuronal cell networks (***Beisbart et al., 2006***) and to determine the direction of elongation in multiphase field models for epithelial tissue (***Mueller et al., 2019***; ***Wenzel and Voigt, 2021***; ***Happel and Voigt, 2024***). However, the mentioned examples exclusively use lower-rank Minkowski tensors $a + b \leq 2$. Higher rank tensors have not been considered in such applications but the theory also guarantees robust description of p-atic orientation for $p = 3, 4, 5, 6, \ldots$. These results hold for smooth contours but also can be extended to polyconvex shapes. Furthermore, known counter-examples for non-convex shapes have very little to no relevance in applications (***Kapfer, 2012***).

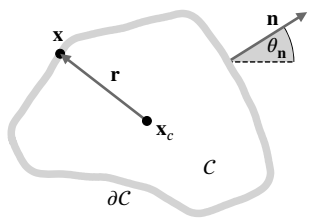

Figure 3. Schematic description of a two-dimensional object $\mathcal{C}$ with contour $\partial\mathcal{C}$. We denote the center of mass with $\mathbf{x}_c$ and vectors from $\mathbf{x}_c$ to points $\mathbf{x}$ on $\partial\mathcal{C}$ with $\mathbf{r}$. The outward-pointing normals are denoted by $\mathbf{n}$, the corresponding angle with the x-axis by $\theta_{\mathbf{n}}$.

Even if all Minkowski tensors carry important geometric information, one type is particularly interesting and will be considered in the following:

$$\boldsymbol{W}_1^{0,p}(\mathcal{C}) = \int_{\delta\mathcal{C}} \underbrace{\mathbf{n} \odot \mathbf{n} \odot \ldots \odot \mathbf{n}}_{\text{p}-times} \,\mathrm{d}\partial\mathcal{C}. \tag{3}$$

In this case, the symmetrized tensor product agrees with the classical tensor product. If applied to polygonal shapes the Minkowski tensors $\boldsymbol{W}_1^{0,p}(\mathcal{C})$ are related to the Minkowski problem for convex polytops (i.e., generalizations of three-dimensional polyhedra to an arbitrary number of dimensions), which states that convex polytops are uniquely described by the outer normals of the edges and the length of the corresponding edge (***Minkowski, 1897***). Several generalizations of this result exist (***Klain, 2004***; ***Schneider, 2013***), which makes the normal vectors a preferable quantity to describe shapes. However, Minkowski tensors contain redundant information, which asks for an irreducible representation. This can be achieved by decomposing the tensor with respect to the rotation group $SO(2)$ (***Kapfer, 2012***; ***Mickel et al., 2013***; ***Klatt et al., 2022***). Following this approach, one can write

$$\boldsymbol{W}_1^{0,p}(\mathcal{C}) = \int_{S^1} \mathbf{u}^p \Psi_{\mathcal{C}}(\mathbf{u}) \,\mathrm{d}\mathbf{u} \quad \text{with} \quad \Psi_{\mathcal{C}}(\mathbf{u}) = \int_{\partial\mathcal{C}} \delta(\mathbf{n}(\mathbf{x}) - \mathbf{u}) \,\mathrm{d}\partial\mathcal{C}, \tag{4}$$

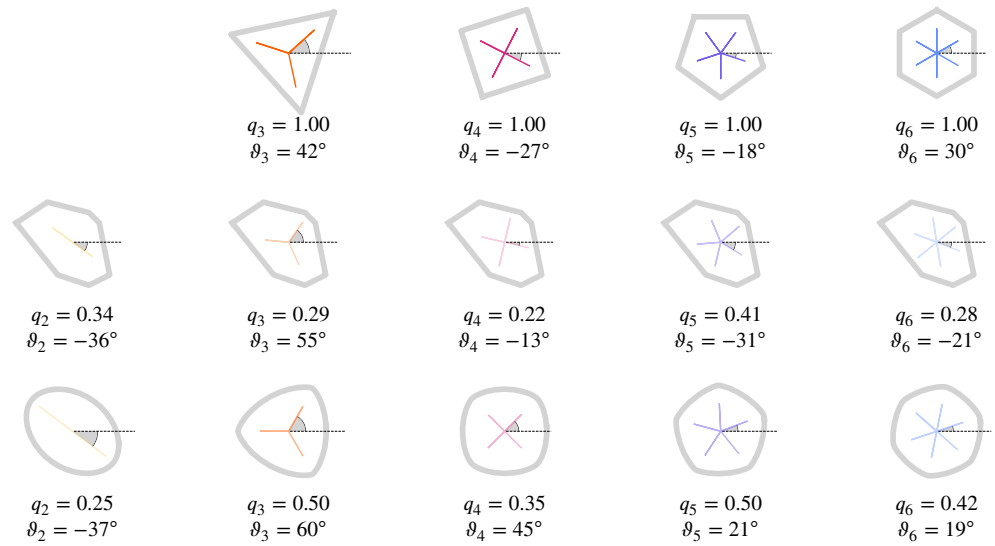

Figure 4. Regular and irregular shapes, adapted from ***Armengol-Collado et al.*** (***2023***) and ***Schaller et al.*** (***2024***), with magnitude and orientation calculated by ***Equation 7***. For regular shapes, the corresponding magnitude of q_p is always 1.0 and the detected angle is the minimal angle of the p-atic orientation with respect to the x-axis. Note that no shape with $q_2 = 1.0$ is shown, as this would be a line. The visualization uses rotationally-symmetric direction fields (known as p-RoSy fields in computer graphics (***Vaxman et al., 2016***)). The brightness scales with the magnitude of the p-atic order, q_p, see colorbars in ***Figure 1***.

with $\Psi_{\mathcal{C}}(\mathbf{u})$ being proportional to the probability density of the normal vectors. Identifying $\mathbf{u} \in S^1$ by the angle θ between $\mathbf{u}$ and the $x-$axis allows to write

$$\Psi_{\mathcal{C}}(\theta) = \sum_{p=-\infty}^{\infty} \psi_p(\mathcal{C}) e^{-ip\theta} \quad \text{with} \quad \psi_p(\mathcal{C}) = \frac{1}{2\pi} \int_0^{2\pi} \Psi_{\mathcal{C}}(\theta) e^{ip\theta} \, \mathrm{d}\theta. \tag{5}$$

The Fourier coefficients $\psi_p(\mathcal{C})$ are the irreducible representations of $\boldsymbol{W}_1^{0,p}(\mathcal{C})$ and can be written as

$$\psi_p(\mathcal{C}) = \frac{1}{2\pi} \int_{\partial\mathcal{C}} e^{ip\theta_{\boldsymbol{n}}} \, \mathrm{d}\partial\mathcal{C}, \tag{6}$$

where $\theta_{\boldsymbol{n}}$ is the orientation of the outward pointing normal $\mathbf{n}$. The phase of the complex number $\psi_p(\mathcal{C})$ contains information about the preferred orientation and the absolute value $|\psi_p(\mathcal{C})|$ is a scalar index. We thus define

$$\vartheta_p(\mathcal{C}) = \frac{1}{p} \arctan 2 \left(\Im\psi_p(\mathcal{C}), \Re\psi_p(\mathcal{C}) \right) + \frac{\pi}{p} \quad \text{and} \quad q_p(\mathcal{C}) = \frac{|\psi_p(\mathcal{C})|}{\psi_0(\mathcal{C})}, \tag{7}$$

with $\Im\psi_p$ and $\Re\psi_p$ the imaginary and real part of ψ_p, respectively, and $\psi_0(\mathcal{C}) = \frac{W_1(\mathcal{C})}{2\pi}$. We have $q_p(\mathcal{C}) \in [0, 1]$ quantifying the strength of p-atic order. ***Figure 4*** illustrates the concept for polygonal and smooth shapes and ***Figure 5*** illustrates the calculation of q_p and ϑ_p at the example of an equilateral triangle. Note that the constant factor of $1/(2\pi)$ in ***Equation 6*** does not influence the result of ***Equation 7*** and is therefore disregarded in ***Figure 5***. Alternative derivations of ***Equation 7*** consider higher order trace-less tensors (***Virga, 2015***; ***Giomi et al., 2022***; ***Armengol-Collado et al., 2023***) generated by the normal $\mathbf{n}$. In this case $\vartheta_p(\mathcal{C})$ (orange triatic director in ***Figure 5*** right) correspond to the eigenvector to the negative eigenvalue and $\vartheta_p(\mathcal{C}) - \pi/p$ (gray triatic director in ***Figure 5*** right) to the eigenvector to the positive eigenvalue. For $p = 2$ this tensor based approach corresponds to the structure tensor (***Mueller et al., 2019***).

As pointed out in the introduction, p-atic orders have already been identified in biological tissue and model systems. However, the way to quantify rotational symmetry in these works differs from the Minkowski tensors. In ***Armengol-Collado et al.*** (***2023***) the cell contour is approximated by a

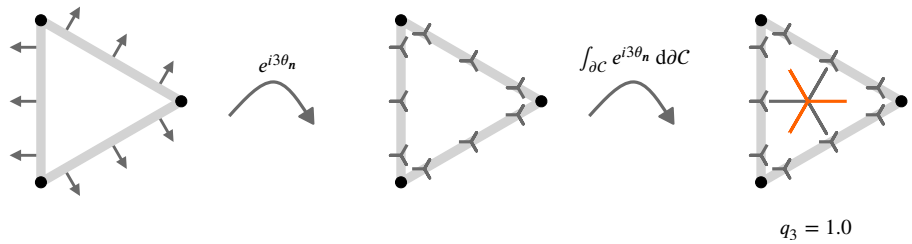

Figure 5. Illustrative description of the definition of q_3 for an equilateral triangle. Considering rotational symmetries under a rotation $120° = 2\pi/3$ means that vectors with an angle of $120°$ or $240°$ are treated as equal. Applied to the normals $\mathbf{n}$ (left), this means that under this rotational symmetry the normals on the three different edges are equal. Mathematically this is expressed through $e^{3i\theta_\mathbf{n}}$ resulting in the triatic director shown instead of the normals $\mathbf{n}$ (middle). One leg of the triatic director always points in the direction as the normal. While only shown for 3 points on each edge, we obtain an orientation with the respective symmetry on every point of the contour ∂C. Considering the line integral along the contour provides the dominating triatic director, shown in the center of mass (right). To get a value between 0.0 and 1.0 for q_3 we normalize this integral with the length of the contour, which corresponds to q_0. As all triatic directors point in the same direction we obtain $q_3 = 1.0$ in this specific example. To be consistent with other approaches we rotate the resulting triatic director by $60° = \pi/3$ leading to the orange triadic director, which is the quantity used for visualization.

polygon with V vertices having coordinates $\mathbf{x}_i$. The considered polygonal shape analysis is based on the shape function

$$\gamma_p(C) = \frac{\sum_{i=1}^{V} |\mathbf{r}_i|^p e^{ip\theta_i}}{\sum_{i=1}^{V} |\mathbf{r}_i|^p}, \tag{8}$$

with $\mathbf{r}_i = \mathbf{x}_i - \mathbf{x}_c$ being the vector from the center of mass $\mathbf{x}_c$ and θ_i being the orientation of the i-th vertex of the polygon with respect to its center of mass. As the center of mass can be computed by $\mathbf{x}_c = \frac{1}{V}\sum_{i=1}^{V} \mathbf{x}_i$ the only input data are the coordinates of the vertices of the V-sides polygon. ***Equation 8*** captures the degree of regularity of the polygon by its amplitude $0 \leq |\gamma_p| \leq 1$ and its orientation ϑ_p which follows as

$$\vartheta_p(C) = \frac{1}{p} \arctan \frac{\Im\gamma_p(C)}{\Re\gamma_p(C)}, \tag{9}$$

with $\Im\gamma_p$ and $\Re\gamma_p$ the imaginary and real part of γ_p, respectively. Instead of the normals $\mathbf{n}$, the descriptor is based on the position vector $\mathbf{r}$. One might be tempted to think that ***Equation 9*** is related to the irreducible representation of $\boldsymbol{W}_1^{p,0}$. This is, however, not the case as the weighting in ***Equation 9*** is done with respect to the magnitude of $\mathbf{r}$, while in $\boldsymbol{W}_1^{p,0}$ the weighting is done with respect to the contour integral. Furthermore, in contrast to the Minkowski tensors, ***Equation 9*** takes into account only the vectors at the vertices and not the vectors along the full cell contour. While this seems to be a technical detail, it has severe consequences. The theoretical basis, which guarantees continuity, no longer holds. This leads to unstable behaviour, as illustrated in ***Figure 6***. While the shape of the polygons is almost identical, there is a jump in γ_3 and γ_4 as we go from four to three vertices. The weighting according to the magnitude cannot cure this, as the magnitude of the shrinking vector is far from zero shortly before this vertex vanishes. In the context of cellular systems, such deformations are a regular occurrence rather than an artificially constructed test case. We will demonstrate the impact while discussing the results and recommend only using robust descriptors such as the Minkowski tensors or their irreducible representations.

We further note that bond order parameters Ψ_p^{bond}, which consider the connection between cells, have also been used as shape descriptors (***Li and Ciamarra, 2018***; ***Durand and Heu, 2019***; ***Pasupalak et al., 2020***). Introduced in ***Nelson and Halperin*** (***1979***), these parameters are

$$\Psi_p^{bond} = \frac{1}{B} \sum_{b=1}^{B} e^{ip\theta_b}, \tag{10}$$

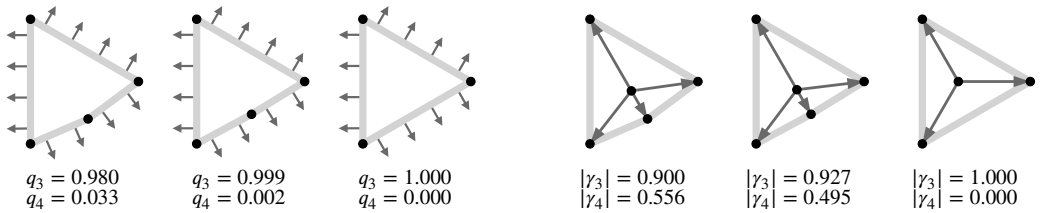

Figure 6. Defining p-atic order for deformable objects requires robust shape descriptors. Shown is the strength of p-atic order for a polygon converging to an equilateral triangle. a) using q_p and b) using γ_p. The considered vectors used in the computations, normals $\mathbf{n}$ of the contour for the Minkowski tensors and $\mathbf{r}_i$ for γ_p, are shown. Note that the choice of the center of mass highly influences the value of γ_p. We here used the described approach following ***Armengol-Collado et al.*** (***2023***).

with B denoting the number of bonds and θ_b the orientation of the bond b. In the context of monolayer tissues, B is understood as the number of neighbors, and θ_b as the orientation of the connection of the center of mass of the current cell with the center of mass of the neighbor b (***Loewe et al., 2020***; ***Monfared et al., 2023***). So cells with the same contour but different neighbor relations lead to different bond order parameters. This characteristic should already disqualify these measures as shape descriptors. However, as discussed in detail in ***Mickel et al.*** (***2013***), they are not robust even for the task they are designed for. We therefore do not discuss them further.

Simulation methods

We consider two modeling approaches, an active vertex model and a multiphase field model. Both have been proven to capture various generic properties of epithelial tissue (***Hakim and Silberzan, 2017***; ***Alert and Trepat, 2020***; ***Moure and Gomez, 2021***). The key aspects of formulations are outlined in ***Box 1*** and ***Box 2***. They refer to (***Koride et al., 2018***; ***Das et al., 2021***; ***Killeen et al., 2022***) and (***Wenzel and Voigt, 2021***; ***Jain et al., 2023***, ***2024b***), respectively. Parameters used within these models are listed in ***Appendix 1 Table 1*** and ***Appendix 1 Table 2***.

The initial configuration for the active vertex model simulations was built by placing N points randomly in a periodic simulation box of length $L \times L$ and ensuring that no two points were within a distance less than r_{cut} from each other. The points were used to create a Voronoi tiling. Typically, such a tiling had cells of very irregular shapes. To make cell shapes more uniform, the centroids of each tile were computed and used as seeds for a new Voronoi tiling. This process was iterated until it converted within the tolerance of 10^{-5}, resulting in a so-called well-centered Voronoi tiling with cells of random shapes but similar sizes. Initial directions of polarity vectors $\hat{\mathbf{n}}_{C_i}$ were chosen at random from a uniform distribution. The initial configuration for the multiphase field model simulations considers a regular arrangement of N cells of equal size in a periodic simulation box of length $L \times L$ with randomly chosen directions of self-propulsion and simulating for several time steps until the cell shapes appear sufficiently irregular. For both models we consider 100 cells and analyse time instances of the evolution.

Experimental setup

Cell culture

Madin-Darby canine kidney (MDCK) cells were cultured in DMEM (DMEM, low glucose, GlutaMAX™ Supplement, pyruvate) supplemented with $10\,\%$ fetal bovine serum (FBS; Gibco) and $100\,\mathrm{U/mL}$ penicillin/streptomycin (Gibco) at $37\,^{\circ}\mathrm{C}$ with $5\,\%$ CO_2. The cell line was tested mycoplasma.

Monolayer preparation

Cells were seeded on glass-bottom dishes (Mattek) pretreated with $10\,\mu\mathrm{g/mL}$ fibronectin human plasma in phosphate buffered saline (PBS, pH 7.4; Gibco). Fibronectin was incubated for $30\,\mathrm{min}$ at $37\,^{\circ}\mathrm{C}$. The initial cell seeding density was sparse. They were imaged approximately 24 hours after, when a confluent monolayer was formed.

Box 1. Active vertex model

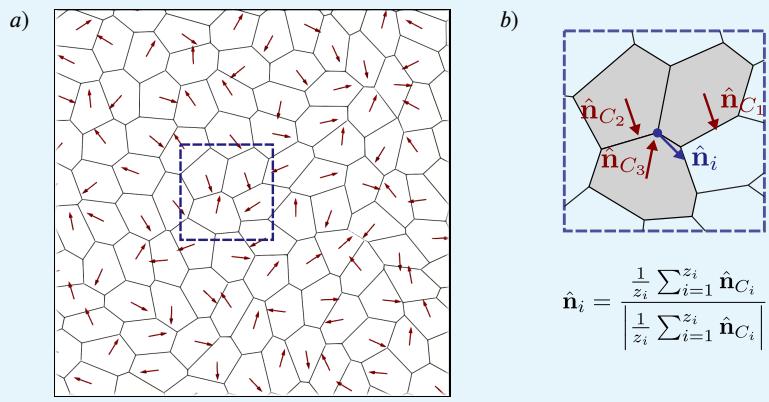

Box 1—figure 1. a) Cell contour of the active vertex model. Red arrows represent the polarity vectors that set each cell's instantaneous direction of self-propulsion. b) Zoom in on a vertex surrounded by three cells showing how the direction of self-propulsion on a vertex is calculated.

The active vertex model is based on models discussed in (***Koride et al., 2018***; ***Das et al., 2021***; ***Killeen et al., 2022***). A confluent epithelial tissue is appreciated as a two-dimensional tiling of a plane with the elastic energy given as (***Honda, 1983***; ***Farhadifar et al., 2007***; ***Honda and Nagai, 2022***)

$$E_{\mathrm{VM}} = \frac{K_A}{2}\sum_C \left(A_C - A_0\right)^2 + \frac{K_P}{2}\sum_C \left(P_C - P_0\right)^2, \tag{11}$$

where A_C and P_C are, respectively, area and perimeter of cell C, A_0 and P_0 are, respectively, preferred area and perimeter, and K_A and K_P are, respectively, area and perimeter moduli. For simplicity, it is assumed that all cells have the same values of A_0, P_0, K_A, and K_P. The model can be made dimensionless by dividing ***Equation 11*** by $e^* = K_A A_0^2$,

$$e_{\mathrm{VM}} = \frac{1}{2}\sum_C \left(a_C - 1\right)^2 + \frac{k_P}{2}\sum_C \left(p_C - p_0\right)^2, \tag{12}$$

where $a_C = A_C/A_0$ (i.e. $l^* = \sqrt{A_0}$ is the unit of length), $p_c = P_C/\sqrt{A_0}$, $k_P = K_P/(K_A A_0)$, and $p_0 = P_0/\sqrt{A_0}$. p_0 is called the shape index, and it has been shown to play a central role in determining if the tissue is in a solid or fluid state (***Bi et al., 2015***).

One can use ***Equation 11*** to find the mechanical force on a vertex i as $\mathbf{F}_i = -\nabla_{\mathbf{r}_i} E_{\mathrm{VM}}$, where $\nabla_{\mathbf{r}_i}$ is the gradient with respect to the position $\mathbf{r}_i$ of the vertex. The expression for $\mathbf{F}_i$ is given in terms of the position of the vertex i and its immediate neighbours (***Tong et al., 2023***), which makes it fast to compute. Furthermore, cells move on a substrate by being noisily self-propelled along the direction of their planar polarity described by a unit-length vector $\hat{\mathbf{n}}_{C_i}$ from which the polarity direction at the vertex $\hat{\mathbf{n}}_i$ is defined, see Box 1 - figure 1 b), where z_i is the number of neighbours of vertex i. It is convenient to write $\hat{\mathbf{n}}_i = \cos(\alpha_i)\mathbf{e}_x + \sin(\alpha_i)\mathbf{e}_y$, where α_i is an angle with the $x-$axis of the simulation box. The equations of motion for vertex i is a force balance between active, elastic, and frictional forces and are given as

$$\dot{\mathbf{r}}_i = v_0\hat{\mathbf{n}}_i + \frac{1}{\gamma_{fr}}\mathbf{F}_i, \quad \dot{\alpha}_i = \xi_i(t), \tag{13}$$

where v_0 is the magnitude of the self-propulsion velocity defined as f_0/γ_{fr}. Furthermore the overdot denotes the time derivative, γ_{fr} is the friction coefficient, f_0 is the magnitude of the self-propulsion force (i.e., the activity), $\xi_i(t)$ is Gaussian noise with $\langle\xi_i(t)\rangle = 0$ and $\langle\xi_i(t)\xi_j(t')\rangle = 2D_{\mathrm{r}}\delta_{ij}\delta(t-t')$, where D_{r} is the rotation diffusion constant and $\langle\cdot\rangle$ is the ensemble average over the noise. Equations of motion can be non-dimensionalised by measuring time in units of $t^* = \gamma_{\mathrm{fr}}/(K_A A_0)$ and force in units of $f^* = K_A A_0^{3/2}$ and integrated numerically using the first-order Euler-Maruyama method with timestep τ.

Box 2. Multiphase field model

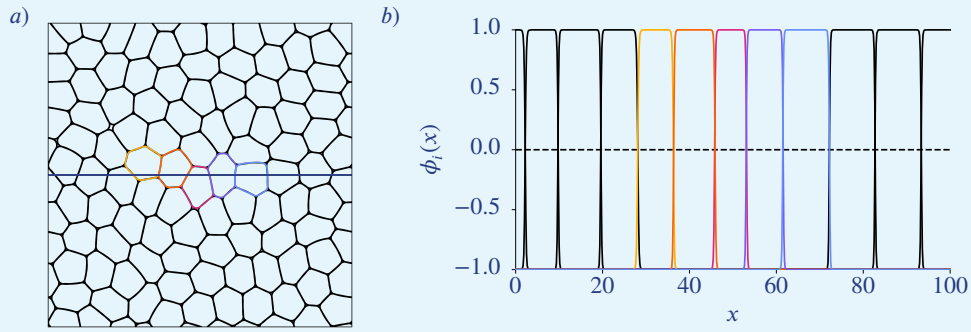

Box 2—figure 1. a) Cell contours of the multiphase field model. b) Corresponding phase field functions along the horizontal line in a). Colours correspond to the once in a).

The multiphase field modelling approach follows ***Wenzel and Voigt*** (***2021***); ***Jain et al.*** (***2023***, 2024b). Each cell is described by a scalar phase field variable ϕ_i with $i = 1, 2, \dots, N$, where the bulk values $\phi_i \approx 1$ denotes the cell interior, $\phi_i \approx -1$ denotes the cell exterior, and with a diffuse interface of width $\mathcal{O}(\epsilon)$ between them representing the cell boundary. The phase field ϕ_i follows the conservative dynamics

$$\partial_t \phi_i + \mathbf{v}_i \cdot \nabla \phi_i = \Delta \frac{\delta \mathcal{F}}{\delta \phi_i}, \tag{14}$$

with the free energy functional $\mathcal{F} = \mathcal{F}_{CH} + \mathcal{F}_{INT}$ containing the Cahn-Hilliard energy

$$\mathcal{F}_{CH} = \frac{1}{Ca} \sum_{i=1}^{N} \int_{\Omega} \left(\frac{\epsilon}{2} \|\nabla \phi_i\|^2 + \frac{1}{4\epsilon} (\phi_i^2 - 1)^2 \right) d\mathbf{x}, \tag{15}$$

where the Capillary number Ca is a parameter for tuning the cell deformability, and an interaction energy consisting of repulsive and attractive parts defined as

$$\mathcal{F}_{INT} = \frac{1}{In} \sum_{i=1}^{N} \int_{\Omega} \sum_{j \neq i} a_r (\phi_i + 1)^2 (\phi_j + 1)^2 - a_a (\phi_i^2 - 1)^2 (\phi_j^2 - 1)^2 d\mathbf{x}, \tag{16}$$

where In denotes the interaction strength, and a_r and a_a are parameters to tune contribution of repulsion and attraction. The repulsive term penalises overlap of cell interiors, while the attractive part promotes overlap of cell interfaces. The relation to former formulations is discussed in ***Happel and Voigt*** (***2024***).

Each cell is self-propelled, and the cell activity is introduced through an advection term. The cell velocity field is defined as

$$\mathbf{v}_i(\mathbf{x}, t) = v_0 \mathbf{e}_i(t) \hat{\phi}_i(\mathbf{x}, t), \tag{17}$$

where v_0 is used to tune the magnitude of activity, $\hat{\phi}_i = \frac{\phi_i + 1}{2}$ and $\mathbf{e}_i = [\cos\theta_i(t), \sin\theta_i(t)]$ is its direction. The migration orientation $\theta_i(t)$ evolves diffusively with a drift that aligns to the principal axis of cell's elongation as $d\theta_i = \sqrt{2D_r} dW_i(t) + \alpha(\beta_i(t) - \theta_i(t)) dt$, where D_r is the rotational diffusivity, W_i is the Wiener process, $\beta_i(t)$ is the orientation of the cell elongation and α controls the time scale of this alignment.

The resulting system of partial differential equations is considered on a square domain with periodic boundary conditions and is solved by the finite element method within the toolbox AMDiS (***Vey and Voigt, 2007***; ***Witkowski et al., 2015***) and the parallelization concept introduced in ***Praetorius and Voigt*** (***2018***) is considered, which allows scaling with the number of cells. We in addition introduce a de Gennes factor in $\mathcal{F}_{CH}$ to ensure $\phi_i \in [-1, 1]$, see ***Salvalaglio et al.*** (***2021***).

Live cell imaging

Samples were imaged using Nikon ECLIPSE Ti microscope equipped with a H201-K-FRAME Okolab chamber, heating system (Okolab) and a CO_2 pump (Okolab) which maintained them at $37\,^{\circ}\mathrm{C}$ and at $5\,\%$ CO_2. Phase microscopy images were taken each 10th minute using a 10× NA=0.3 Plan Fluor objective and Andor Neo 5.5 sCMOS camera.

Image analysis

The time-series were xy-drift corrected using Fast4DReg plugin ***Laine et al.*** (***2019***), ***Pylvänäinen et al.*** (***2022***) in FIJI. Cells were segmented and tracked using the python module CellSegmentationTracker (https://github.com/simonguld/CellSegmentationTracker), which utilizes both Cellpose ***Stringer et al.*** (***2021***) and Trackmate ***Tinevez et al.*** (***2017***). A Cellpose model was trained by manual segmentation of the phase contrast images.

Results

Quantifying orientational order in biological tissues can be realized by Minkowsky tensors. The orientation ϑ_p and the strength of p-atic order q_p in ***Equation 7*** can be computed for any integer p. These quantities describe how cell shapes align with specific rotational symmetries. A recurring challenge in the field is determining whether q_p values for different p can be meaningfully compared. This question is particularly important for interpreting nematic (q_2) and hexatic (q_6) orders, which describe distinct symmetries but often coexist in biological systems. However, a direct comparison is problematic as q_2 and q_6 reveal significant differences in their ranges: $q_2 = 1.0$ represents an idealized line shape that is unattainable for cells, while $q_6 = 1.0$ corresponds to a perfect hexagon observed in experiments and simulations. To further address this, we analyze simulation data from two computational models, examining how deformability and activity—key determinants of tissue mechanics—affect q_p values and their interplay. We employ the active vertex model and the multiphase field model, both of which incorporate activity and deformability. These two parameters are recognized as crucial for capturing the coarse-grained properties of confluent tissues (***Jain et al., 2023***, ***2024b***). By leveraging these complementary frameworks, we ensure that our conclusions are robust across model-specific assumptions and parameter regimes. This dual approach allows us to systematically investigate how these models capture tissue behavior, particularly regarding cell shape variability and resulting p-atic orders.

In the active vertex model, deformability is controlled by the target shape index p_0, reflecting the balance between cell-cell adhesion and cortical tension. The multiphase field model, by contrast, encodes deformability through the capillary number Ca, which directly incorporates cortical tension. Although these models differ conceptually, both have been validated in studies of cell monolayer mechanics, including solid-liquid transitions, neighbor exchange dynamics, and stress profiles (***Fletcher et al., 2014***; ***Alt et al., 2017***; ***Li et al., 2019***; ***Balasubramaniam et al., 2021***; ***Wenzel and Voigt, 2021***; ***Sknepnek et al., 2023***; ***Melo et al., 2023***). Importantly, the active vertex model enforces confluency by design, while the multiphase field model approximates it through dynamic cell-cell interactions, leading to differences in topological rearrangements and cell shape representations.

We vary activity strength (v_0), the shape index (p_0), and the capillary number (Ca), ensuring all parameter combinations remain in the fluid regime. Fluidity was confirmed using metrics such as the mean square displacement (MSD) (***Loewe et al., 2020***), neighbor number variance (***Wenzel and Voigt, 2021***), and the self-intermediate scattering function (***Bi et al., 2016***). Using Minkowski tensors, we computed ϑ_p and q_p values as described in ***Equation 7***, focusing on $p = 2$ and $p = 6$ due to their biological relevance. In solid-like states, such as hexagonal cellular arrangements, hexatic order ($p = 6$) is the appropriate descriptor, as hexagons exhibit $60^{\circ} = 2\pi/6$ rotational symmetry. Hexatic order has been extensively studied in biological systems (***Li and Ciamarra, 2018***; ***Durand and Heu, 2019***; ***Pasupalak et al., 2020***), and its importance in cellular organization is well-documented. In fluid-like states, cells often become elongated, exhibiting nematic order ($p = 2$), characterized by $180^{\circ} = 2\pi/2$ rotational symmetry. Elongated cell shapes are also common in

specific cell types, such as fibroblasts. Quantifying nematic order using q_2 is particularly relevant, as nematic configurations and defects have been linked to critical biological processes, including hydra morphogenesis (***Maroudas-Sacks et al., 2021***) and cell death (***Saw et al., 2017***).

Independence of q_2 and q_6

Recent studies suggest a hexatic-nematic crossover in epithelial tissues, where hexatic order dominates at small scales and nematic order prevails at larger scales (***Eckert et al., 2023***; ***Armengol-Collado et al., 2023***, ***2024***). To explore this relationship, we examine the distribution of (q_2, q_6) values across deformability-activity parameter pairs in both models (***Figure 7***). Despite structural

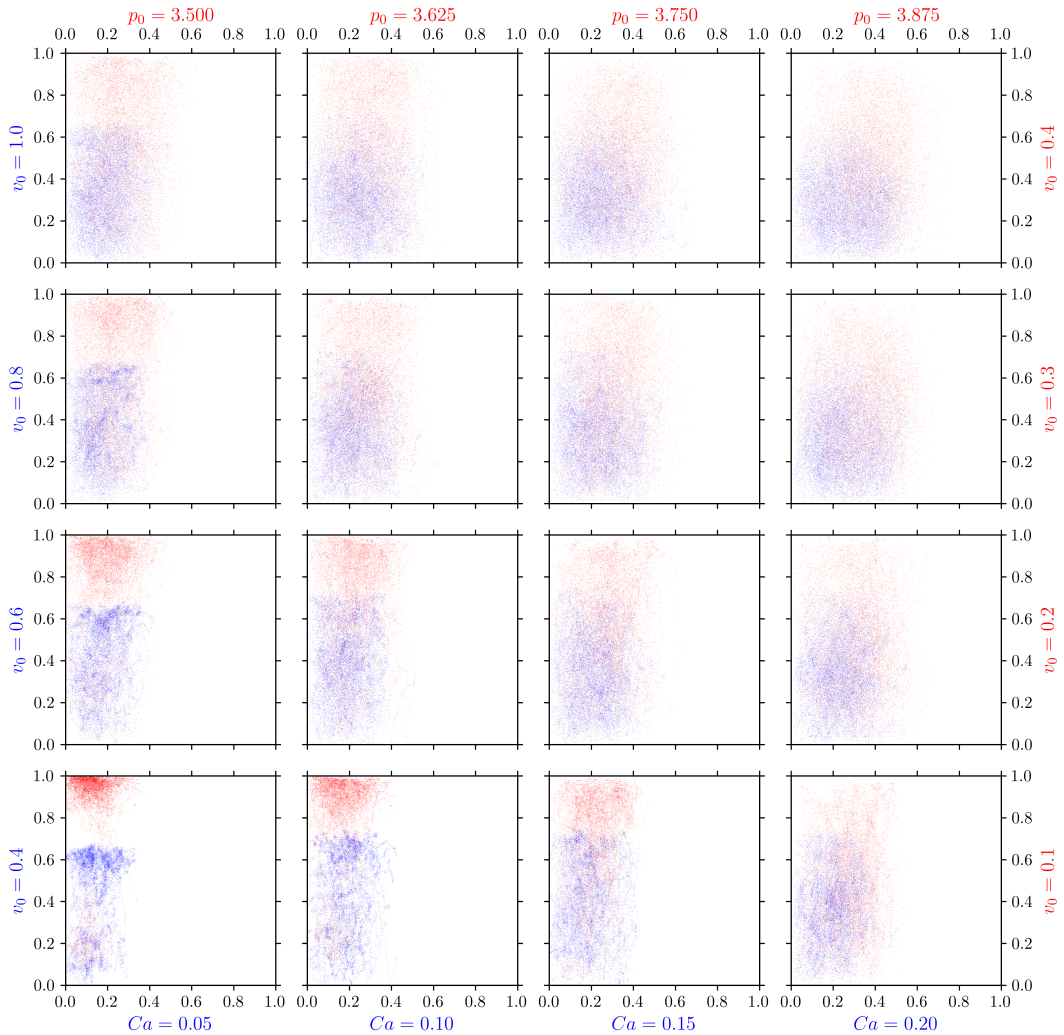

Figure 7. Nematic ($p = 2$) and hexatic ($p = 6$) order are independent of eachother. q_6 (y-axis) versus q_2 (x-axis) for all cells in the multiphase field model (blue) and active vertex model (red). For each cell and each timestep we plot one point (q_2, q_6). Each panel corresponds to specific model parameters; Ca and v_0 for multiphase field model, and p_0 and v_0 for the active vertex model, representing deformability and activity, respectively.

differences between the models, both show consistent trends. Closer examination shows that in near-solid regimes (***Figure 7*** lower left), q_2 and q_6 values cluster tightly due to restricted shape fluctuations. However, even in this regime, small q_2 values can correspond to either small or large q_6 values, and vice versa. In more fluid-like regimes, with higher activity and higher deformability (***Figure 7*** upper right), q_2 and q_6 values become highly scattered. Each q_2 value spans a broad range of q_6 values, and vice versa, demonstrating their independence. These findings underscore that q_p

values for different p measure distinct aspects of cell shape anisotropy and cannot be meaningfully compared directly.

This conclusion also holds on larger length scales. In order to test the hypothesis of a hexatic-nematic crossover at larger length scales (***Armengol-Collado et al., 2023***) we consider a coarse-graining of q_2 and q_6 across spatial domains. Details are described in ***Appendix 2***. ***Appendix 2 - Figure 13*** and ***Appendix 2 -Figure 14*** show the results for the active vertex model and the multiphase field model, respectively. The results show no consistent trends indicative of a crossover, regardless of the considered model and coarse-graining radius. Instead, the apparent convergence of Q_2 and Q_6 values (coarse-grained values of q_2 and q_6) with increasing activity or deformability simply reflects the same trends observed at the individual cell scale.

Dependence of q_p on activity and deformability

The previous analysis demonstrated that comparing q_p across different values of p is not meaningful. However, fixing p and exploring q_p under varying physical conditions offers valuable insights into how tissue properties such as activity and deformability influence cell shape and orientational order. We again focus on nematic ($p = 2$) and hexatic ($p = 6$), as shown in ***Figure 8*** and ***Figure 9***. Additional results for $p = 3, 4, 5$ are provided in ***Figure 8—figure Supplement 1–Figure 8—figure Supplement 3*** (fixed activity) and ***Figure 9—figure Supplement 1–Figure 9—figure Supplement 3*** (fixed deformability). In all plots all cells and all time steps are considered. In ***Figure 8***, we vary deformability (p_0 in the active vertex model and Ca in the multiphase field model) while keeping the activity v_0 constant. Results are presented for the active vertex model (left column) and the multiphase field model (right column). Activity increases from bottom to top rows. Both models show qualitatively similar trends in the probability density functions (PDFs) of q_2 and q_6. For $p = 6$, increasing deformability shifts the PDF of q_6 to the left, indicating lower mean values. In contrast, for $p = 2$, higher deformability leads to higher q_2 values, reflected in a rightward shift of the PDF. This trend is confirmed by the mean values, shown as a function of deformability (p_0 and Ca, respectively) in the inlets. Additionally, the PDFs broaden with increasing deformability, and this effect is more pronounced at lower activity levels. A notable difference between the models is the range of q_p values. In the multiphase field model, q_p rarely exceeds 0.8 due to the smoother, more rounded cell shapes, whereas the active vertex model often produces higher q_p values. In ***Figure 9***, deformability is held constant while activity v_0 is varied. Results are again shown for the active vertex model (left column) and the multiphase field model (right column), with increasing activity indicated by brighter colors. Deformability increases from bottom to top rows. The trends mirror those observed in ***Figure 8***. Increasing activity reduces the mean value of q_6 while increasing q_2, see inlets. The effects of activity are more pronounced at lower deformabilities; at higher deformabilities, differences between parameter regimes diminish. The results agree qualitatively with the ones obtained for the measures $|\gamma_2|$ and $|\gamma_6|$ reported in (***Armengol-Collado et al., 2023***, Extended Data Fig. 3). Note that in the calculation of γ_p every cell is approximated by a polygon. Therefore, also for the multiphase field model the obtained values range up to 1.0. The overall behavior of q_2 and q_6 is summarized in ***Figure 10***, which shows the mean values $\overline{q_2}$ and $\overline{q_6}$ as functions of activity and deformability. For both models:

- $\overline{q_2}$ increases with higher activity or deformability
- $\overline{q_6}$ decreases with higher activity or deformability.

This behaviour is consistent with a trend towards nematic order in more dynamic regimes and toward hexagonal order in more constrained, less dynamic regimes. The first is further confirmed by recent findings in analysing T1 transitions and their effect on cell shapes ***Jain et al.*** (***2024a***). These studies suggest that cells transiently elongate when they are undergoing T1 transitions. As the number of T1 transitions increases with activity or deformability ***Jain et al.*** (***2024b***) this elongation contributes to the observed behavior. The second is consistent with the emergence of hexagonal

arrangements in solid-like states. Corresponding results for $p = 3, 4, 5$ are shown in ***Figure 10—figure Supplement 1***.

Comparison with experiments

Next, we apply shape descriptor framework to experiments on epithelial cells. We consider a monolayer of Madine-Derby-Canine-Kidney (MDCK) cells. We consider two types of cell monolayers: MDCK wild type cells and MDCK E-cad KO cells, which have the E-cadherin protein removed. These E-cad KO cells have weaker cell-cell adhesion strengths and previous studies have shown that compared to wild-type cells, the E-cad KO cells have lower velocities, same spreading area, higher aspect ratio, and higher stiffness ***Balasubramaniam et al.*** (***2021***); **?**. The slower movement of E-cad KO cells compared to the wild-type cells suggest their lower activity, and their higher stiffness can be intepreted as having lower deformability compared to the wild-type cells. However, care must be taken in directly comparing the two cell types and directly comparing to simulation results , as the key parameters varied in simulations—cell activity and deformability—are difficult to manipulate in isolation in experiments. One complicating factor is the strong dependence of cell shape on cell density, as previously reported (***Eckert et al., 2023***). Higher cell densities generally lead to rounder cell shapes, which we confirmed in two distinct experimental setups (see ***Figure 11***). For both wild-type MDCK cells and E-cadherin knockout variants, increased cell density corresponded to lower mean values of q_2, consistent with rounder cell geometries. For higher values of q_p, however, this density-dependent effect was less pronounced. A plausible explanation lies in the geometry of shapes for larger q_p. Rounded shapes close to a circle can yield relatively high q_p values for certain p, such as the example shown in the third row of ***Figure 4***. Distinguishing such shapes from perfect circles requires highly accurate data, which can be difficult to obtain in experimental imaging, potentially masking density-dependent effects for $p = 6$.

Importantly, due to the substantial differences in cell density between wild-type cells and E-cadherin knockout variants, direct comparisons between these two experimental conditions would be unjustifiable. Density influences cell shape too strongly to isolate other effects in these datasets. Despite these limitations, we observed qualitative agreement between experimental and computational results regarding the independence of q_2 and q_6 (see ***Figure 12***). Both measures appear to be unrelated, reinforcing the conclusion that nematic ($p = 2$) and hexatic ($p = 6$) order describe distinct aspects of cell shape and alignment. Consequently, comparing q_2 and q_6 directly is not meaningful, whether in simulations nor in experiments.

Sensitivity of the results on the considered shape descriptor

In order to demonstrate that other methods, such as polygonal shape analysis ***Armengol-Collado et al.*** (***2023***) fail to capture the nuances of irregular cell shapes we also use ***Equation 8*** as a shape descriptor for the considered datasets. For the experimental data and the multiphase field model this first requires an approximation of the cell shape by a polygon. For finding the vertices of the polygon we consider the Voronoi interface method (***Saye and Sethian, 2011***, ***2012***), see ***Appendix 3***. The corresponding figures to ***Figure 1***, ***Figure 2*** and ***Figure 4*** are shown in ***Appendix 3 Figure 16***, ***Appendix 3 Figure 17*** and ***Appendix 3 Figure 15***, respectively. While already these results show quantitative differences, the failure of the approach can best be seen in the qualitative difference between ***Figure 10*** and the corresponding results in ***Appendix 3 Figure 18***, which, instead of the monotonic trend for activity and deformabilty, exhibit nonmonotonic trends, peaking at intermediate values of activity or deformability. These divergences highlight the limitations of γ_p in capturing consistent patterns and emphasize the need for stable, reliable shape descriptors like the Minkowski tensors.

For completeness we also provide the corresponding figures to ***Figure 7*** and ***Figure 13*** in ***Appendix 3 Figure 19*** and ***Appendix 3 Figure 20***, respectively. We hereby only consider the active vertex model. The results are similar to the once obtained using the Minkowski tensors and confirm the independence of p-atic order for different symmetries.

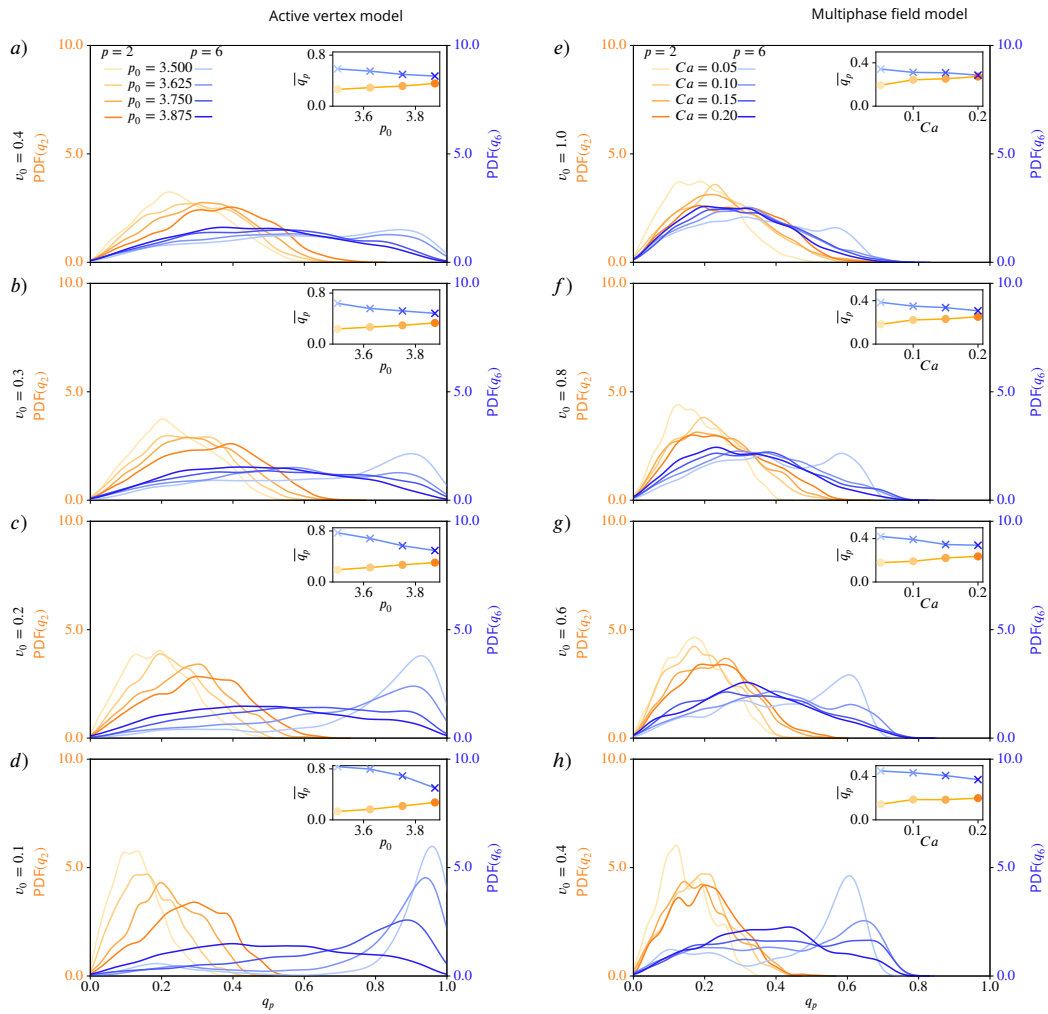

Figure 8. Nematic ($p = 2$) and hexatic ($p = 6$) order depend on deformability of the cells. Probability distribution functions (PDFs) for q_2 (shades of orange) and q_6 (shades of blue), using kde-plots, for varying deformability p_0 or Ca and fixed activity v_0. Inlets show mean values of q_2 and q_6 as function of deformability. a) - d) active vertex model, e) - h) multiphase field model for decreasing activity.

Figure 8—figure supplement 1. PDFs for q_3 using kde-plots, for varying deformability p_0 or Ca and fixed activity v_0. Inlets show mean values of q_3 as function of deformability. a) - d) active vertex model, e) - h) multiphase field model for descreasing activity.

Figure 8—figure supplement 2. PDFs for q_4 using kde-plots, for varying deformability p_0 or Ca and fixed activity v_0. Inlets show mean values of q_4 as function of deformability. a) - d) active vertex model, e) - h) multiphase field model for decreasing activity.

Figure 8—figure supplement 3. PDFs for q_5 using kde-plots, for varying deformability p_0 or Ca and fixed activity v_0. Inlets show mean values of q_5 as function of deformability. a) - d) active vertex model, e) - h) multiphase field model for decreasing activity.

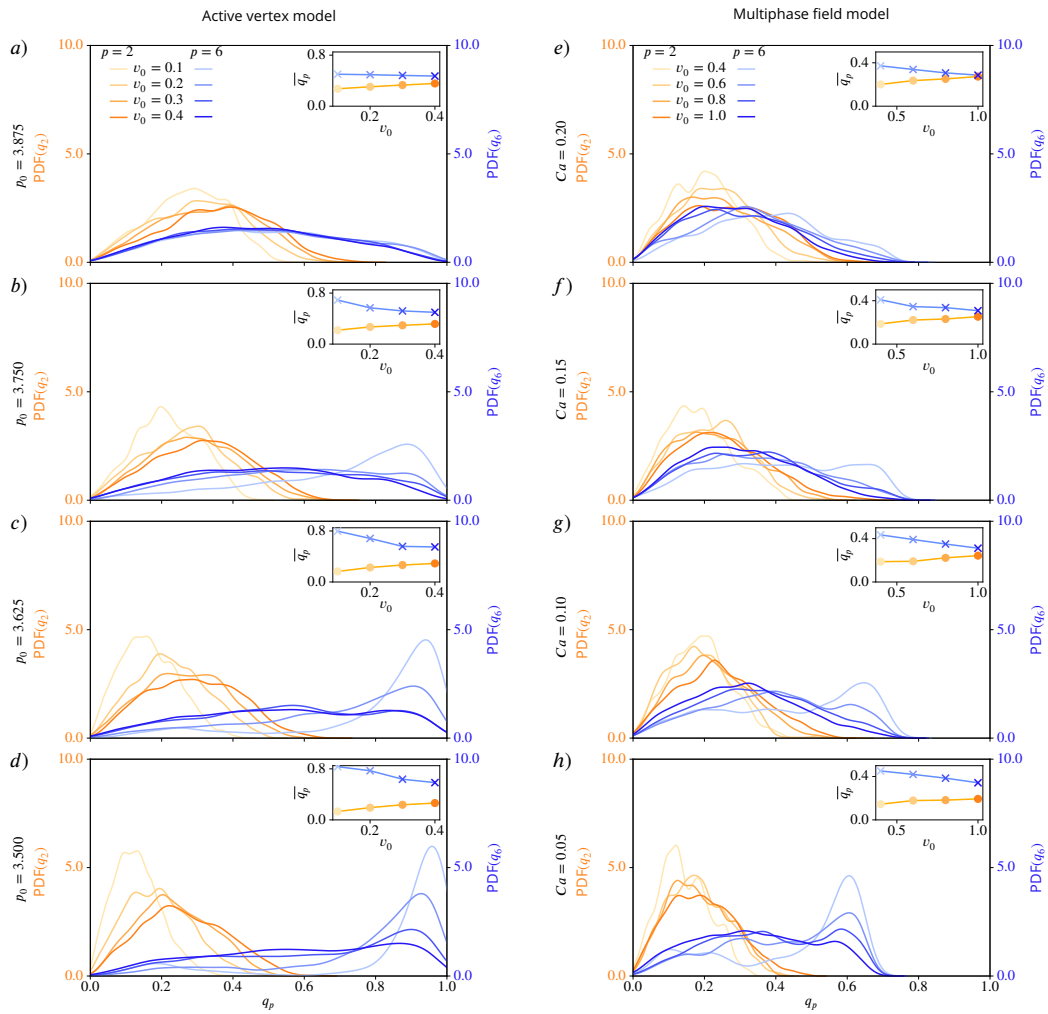

Figure 9. Nematic ($p = 2$) and hexatic ($p = 6$) order depend on activity of the cells. Probability distribution functions (PDFs) for q_2 (shades of orange) and q_6 (shades of blue), using kde-plots, for varying activity v_0 and fixed deformability p_0 or Ca. Inlets show mean values of q_2 and q_6 as function of activity. a) - d) active vertex model and e) - h) multiphase field model for decreasing deformability.

Figure 9—figure supplement 1. PDFs for q_3 using kde-plots, for varying activity v_0 and fixed deformability p_0 or Ca. Inlets show mean values of q_3 as function of activity. a) - d) active vertex model and e) - h) multiphase field model for decreasing deformability.

Figure 9—figure supplement 2. PDFs for q_4 using kde-plots, for varying activity v_0 and fixed deformability p_0 or Ca. Inlets show mean values of q_4 as function of activity. a) - d) active vertex model and e) - h) multiphase field model for decreasing deformability.

Figure 9—figure supplement 3. PDFs for q_5 using kde-plots, for varying activity v_0 and fixed deformability p_0 or Ca. Inlets show mean values of q_5 as function of activity. a) - d) active vertex model and e) - h) multiphase field model for decreasing deformability.

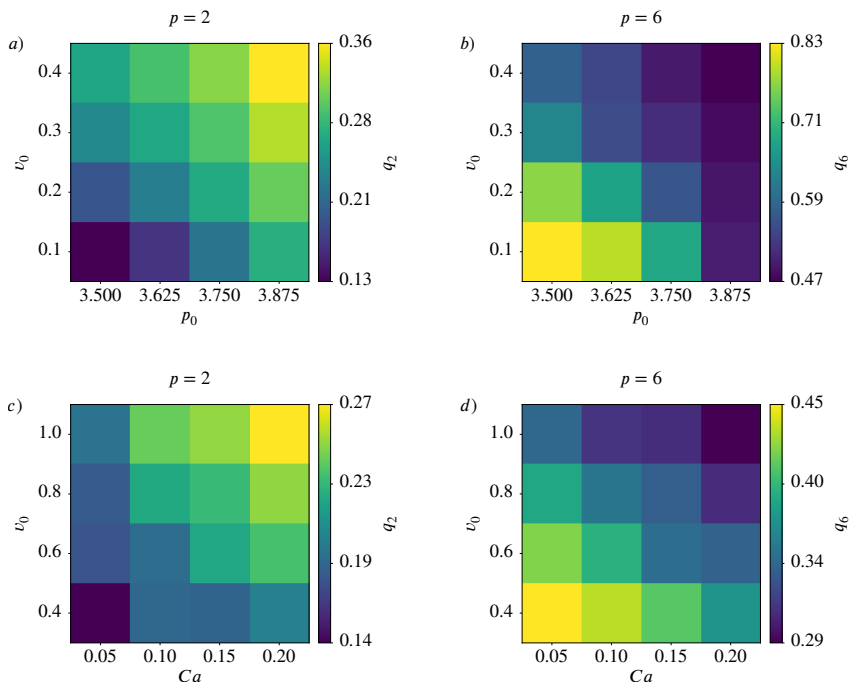

Figure 10. Nematic ($p = 2$) and hexatic ($p = 6$) order depend on activity and deformability of the cells. Mean value $\overline{q_p}$ for $p = 2$ (left) and $p = 6$ (right) as function of deformability p_0 or Ca and activity v_0 for active vertex model (a) and b)) and multiphase field model (c) and d)).

Figure 10—figure supplement 1. Mean value $\overline{q_p}$ for $p = 3$ (left), $p = 4$ (middle) and $p = 5$ (right) as function of deformability p_0 or Ca and activity v_0 for active vertex model (a) - c)) and multiphase field model (d) - f)).

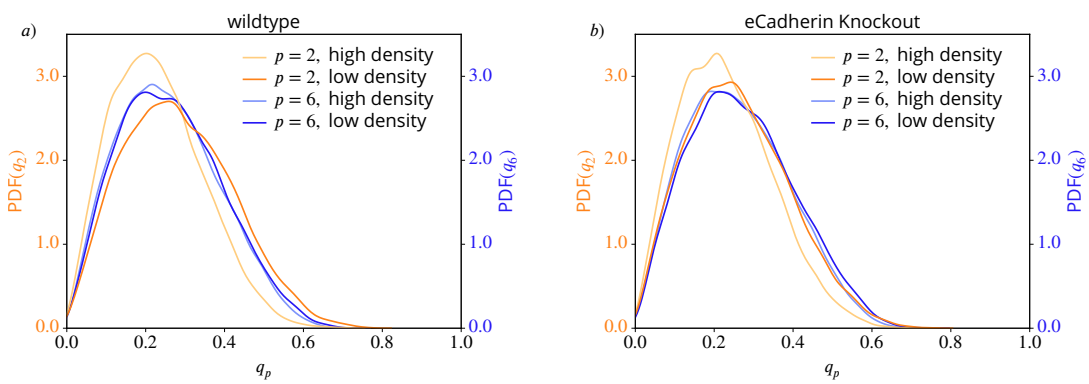

Figure 11. In experimental system of MDCK cells, nematic ($p = 2$) and hexatic ($p = 6$) order respond differently to change in cell density. Probability distribution functions (PDFs) using kde-plots, for q_2 (orange shaded) and q_6 (blue shaded) for different densities in a) wildtype MDCK cell monolayer and b) E-cadherin knockout cell monolayer.

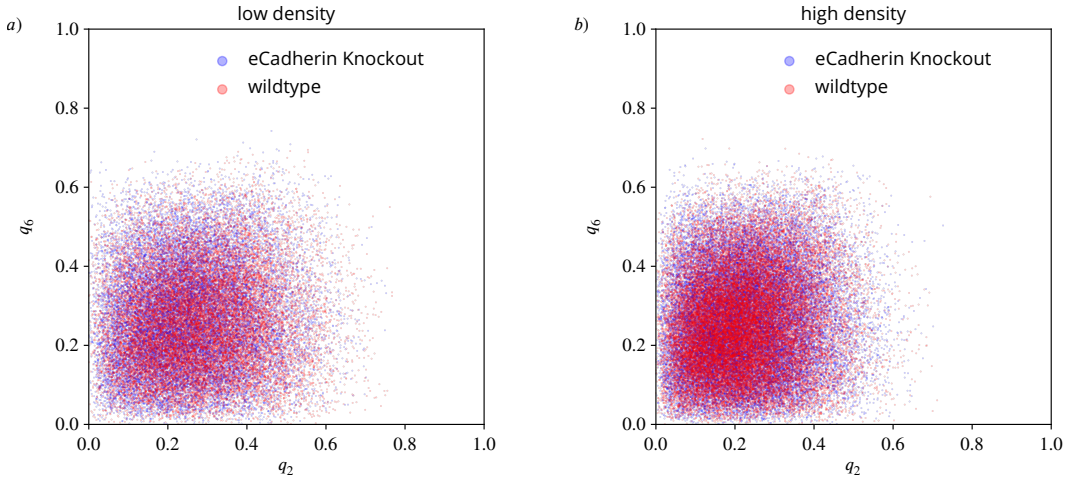

Figure 12. In experimental system of MDCK cells nematic ($p = 2$) and hexatic ($p = 6$) order are independent of eachother for different cell densities and different cell-cell adhesion strengths. q_6 (y-axis) versus q_2 (x-axis) for different densities a) low density and b) high density, for wildtype MDCK cell monolayer and E-cadherin knockout cell monolayer. For each cell and each timestep we plot one point (q_2, q_6).The E-cadherin cells lack an adhesion protein and have therefore weaker cell-cell adhesions.

Discussion

In this study, we introduced Minkowski tensors as a robust and versatile tool for quantifying p-atic order in multicellular systems, particularly in scenarios involving rounded or irregular cell shapes. By applying this framework to extensive datasets from two distinct computational models—the active vertex model and the multiphase field model—we identified universal trends: increasing activity and deformability of the cells enhance nematic order ($p = 2$) while diminishing hexatic order ($p = 6$). The consistency of these findings across two models, despite their inherent differences, underscores the generality and relevance of our results.

While various shape characterization methods, such as the bond order parameter (***Loewe et al., 2020***; ***Monfared et al., 2023***) and the shape function γ_p (***Armengol-Collado et al., 2023***), have been explored in the literature, we demonstrated that the choice of shape descriptor significantly impacts the conclusions drawn. Applying γ_p to data from the active vertex model revealed qualitative discrepancies: for $p = 2$, γ_p and q_p behaved similarly, but for $p = 6$, γ_p exhibited significant changes. Such divergences, together with limited mathematical foundations, highlight the limitations of γ_p in capturing consistent patterns and emphasize the need for stable, reliable shape measures like the Minkowski tensors. In contrast to the bond order parameter or the shape function γ_p the stability of Minkowski tensors can be mathematically justified. We have further demonstrated why bond order parameter or the shape function γ_p fail in certain situations. This finding is not merely a technical nuance; the choice of shape detection method fundamentally influences the interpretation of p-atic order. Consequently, selecting a robust shape descriptor is critical for obtaining meaningful and reproducible insights into orientational order in multicellular systems.

A critical question in the literature has been whether shape measures for different p-atic orders can be directly compared. While some studies have suggested relationships between γ_2 and γ_6 (***Armengol-Collado et al., 2023***), our results refute this notion. We demonstrated that measures like q_2 and q_6 capture fundamentally distinct aspects of cell shape and alignment, and comparing them directly is both mathematically and biologically misleading. We further tested the hypothesis of a hexatic-nematic crossover at larger length scales by coarse-graining q_2 and q_6 across spatial domains. The results showed no consistent trends indicative of a crossover, regardless of the coarse-graining strategy and the considered model. Instead, the apparent convergence of Q_2 and Q_6 values (coarse-grained values of q_2 and q_6) with increasing activity or deformability simply reflected the same trends observed at the individual cell scale. This reinforces the conclusion that comparisons of p-atic orders across different p lack a robust basis and that claims of crossovers require careful reconsideration.

Our findings suggest that p-atic orders should be studied independently across length scales, as they describe complementary aspects of cellular organization. The coexistence of distinct orientational orders emphasized in different studies—such as nematic ($p = 2$) (***Duclos et al., 2017***; ***Saw et al., 2017***; ***Kawaguchi et al., 2017***), tetratic ($p = 4$) (***Cislo et al., 2023***), and hexatic ($p = 6$) (***Li and Ciamarra, 2018***)—is not contradictory but highlights the rich, multifaceted nature of cellular organization. Rather than searching for a single dominant order, future research should focus on the interplay of different p-atic orders and their associated defects. This suggests to not only consider p-atic liquid crystal theories ***Giomi et al.*** (***2022***) for one p, but combinations of these models for various p's. Understanding how these orders interact may reveal how they collectively regulate morphogenetic processes.

Connecting p-atic orders to biological function remains a critical avenue for exploration. While the mathematical independence of q_2, q_6, and other shape measures precludes the identification of a universal dominant order, biological systems may exhibit context-dependent preferences. For example, a specific p-atic order might correlate with or drive a key morphogenetic event. Investigating these connections could yield insights into how tissues achieve functional organization and adapt to environmental cues. As such, while it is difficult to speak of dominating orders from a mathematical point of view, there could be a dominating order from a biological point of view,

meaning the p-atic order connected to the governing biological process.

Acknowledgments

We acknowledge fruitful discussions with Björn Böttger and Brendan Tobin. HJ acknowledges funding by the European Union's Horizon 2020 research and innovation programme under the Marie Skłodowska-Curie grant agreement No. 945371. RS acknowledges support from the UK Engineering and Physical Sciences Research Council (Award EP/W023946/1). AD acknowledges funding from the Novo Nordisk Foundation (grant No. NNF18SA0035142 and NERD grant No. NNF21OC0068687), Villum Fonden (grant No. 29476), and the European Union (ERC, PhysCoMeT, 101041418). AV acknowledges funding from the German Research Foundation (Award FOR3013 "Vector- and tensor-valued surface PDEs") and computing resources provided by JSC through MORPH and by ZIH through WIR. Views and opinions expressed are however those of the authors only and do not necessarily reflect those of the European Union or the European Research Council. Neither the European Union nor the granting authority can be held responsible for them.

References

Alert R, Trepat X. Physical models of collective cell migration. Annual Review of Condensed Matter Physics. 2020; 11:77–101.

Alesker S. Description of continuous isometry covariant valuations on convex sets. Geometriae Dedicata. 1999; 74:241–248.

Alt S, Ganguly P, Salbreux G. Vertex models: from cell mechanics to tissue morphogenesis. Philosophical Transactions of the Royal Society B: Biological Sciences. 2017; 372(1720):20150520.

Armengol-Collado JM, Carenza LN, Eckert J, Krommydas D, Giomi L. Epithelia are multiscale active liquid crystals. Nature Physics. 2023; 19:1773–1779.

Armengol-Collado JM, Carenza LN, Giomi L. Hydrodynamics and multiscale order in confluent epithelia. eLife. 2024; 13:e86400.

Balasubramaniam L, Doostmohammadi A, Saw TB, Narayana GHNS, Mueller R, Dang T, Thomas M, Gupta S, Sonam S, Yap AS, Toyama Y, Mège RM, Yeomans JM, Ladoux B. Investigating the nature of active forces in tissues reveals how contractile cells can form extensile monolayers. Nature Materials. 2021; 20(8):1156–1166.

Beisbart C, Barbosa MS, Wagner H, Costa LdF. Extended morphometric analysis of neuronal cells with minkowski valuations. The European Physical Journal B. 2006; 52:531–546.

Beisbart C, Dahlke R, Mecke K, Wagner H. Vector- and tensor-valued descriptors for spatial patterns. In: Mecke K, Stoyan D, editors. *Morphology of Condensed Matter: Physics and Geometry of Spatially Complex Systems* Berlin, Heidelberg: Springer Berlin Heidelberg; 2002.p. 238–260.

Bernard EP, Krauth W. Two-step melting in two dimensions: first-order liquid-hexatic transition. Physical Review Letters. 2011; 107:155704.

Bi D, Yang X, Marchetti MC, Manning ML. Motility-driven glass and jamming transitions in biological tissues. Physical Review X. 2016; 6:021011.

Bi D, Lopez J, Schwarz JM, Manning ML. A density-independent rigidity transition in biological tissues. Nature Physics. 2015; 11(12):1074–1079.

Bladon P, Frenkel D. Dislocation unbinding in dense two-dimensional crystals. Physical Review Letters. 1995; 74:2519–2522.

Bowick MJ, Manyuhina OV, Serafin F. Shapes and singularities in triatic liquid-crystal vesicles. Europhysics Letters. 2017; 117(2):26001.

Cislo DJ, Yang F, Qin H, Pavlopoulos A, Bowick MJ, Streichan SJ. Active cell divisions generate fourfold orientationally ordered phase in living tissue. Nature Physics. 2023; 19(8):1201–1210.

Das A, Sastry S, Bi D. Controlled neighbor exchanges drive glassy behavior, intermittency, and cell streaming in epithelial tissues. Physical Review X. 2021; 11(4):041037.

Duclos G, Erlenkämper C, Joanny JF, Silberzan P. Topological defects in confined populations of spindle-shaped cells. Nature Physics. 2017; 13(1):58–62.

Durand M, Heu J. Thermally driven order-disorder transition in two-dimensional soft cellular systems. Physical Review Letters. 2019; 123(18):188001.

Eckert J, Ladoux B, Mège RM, Giomi L, Schmidt T. Hexanematic crossover in epithelial monolayers depends on cell adhesion and cell density. Nature Communications. 2023; 14(1):5762.

Farhadifar R, Röper JC, Aigouy B, Eaton S, Jülicher F. The influence of cell mechanics, cell-cell interactions, and proliferation on epithelial packing. Current biology. 2007; 17(24):2095–2104.

Fletcher AG, Osterfield M, Baker RE, Shvartsman SY. Vertex models of epithelial morphogenesis. Biophysical Journal. 2014; 106(11):2291–2304.

Gasser U, Eisenmann C, Maret G, Keim P. Melting of crystals in two dimensions. ChemPhysChem. 2010; 11(5):963–970.

Giomi L, Toner J, Sarkar N. Hydrodynamic theory of p-atic liquid crystals. Physical Review E. 2022; 106(2):024701.

Hadwiger H. Vorlesungen über Inhalt, Oberfläche und Isoperimetrie. Springer Berlin Heidelberg; 1975.

Hakim V, Silberzan P. Collective cell migration: a physics perspective. Reports on Progress in Physics. 2017; 80:076601.

Halperin BI, Nelson DR. Theory of two-dimensional melting. Physical Review Letters. 1978; 41:121–124.

Happel L, Voigt A. Coordinated motion of epithelial layers on curved surfaces. Physical Review Letters. 2024; 132:078401.

Honda H. Geometrical models for cells in tissues. International review of cytology. 1983; 81:191–248.

Honda H, Nagai T. Mathematical models of cell-based morphogenesis. Springer; 2022.

Hug D, Schneider R, Schuster R. The space of isometry covariant tensor valuations. St Petersburg Mathematical Journal. 2007 02; 19:137–158.

Hug D, Schneider R, Schuster R. Integral geometry of tensor valuations. Advances in Applied Mathematics. 2008; 41(4):482–509.

Jain HP, Hu RDJG, Angheluta L. Emergent directional migration due to interplay between cell shape and T1 transitions. Under review. 2024; .

Jain HP, Voigt A, Angheluta L. Robust statistical properties of T1 transitions in a multi-phase field model of cell monolayers. Scientific Reports. 2023; 13(1):10096.

Jain HP, Voigt A, Angheluta L. From cell intercalation to flow, the importance of T1 transitions. Physical Review Research. 2024; 6(3):033176.

Kapfer S. Morphometry and Physics of Particulate and Porous Media. PhD thesis, FAU Erlangen-Nürnberg; 2012.

Kapfer SC, Mickel W, Mecke K, Schröder-Turk GE. Jammed spheres: Minkowski tensors reveal onset of local crystallinity. Physical Review E. 2012; 85:030301.

Kawaguchi K, Kageyama R, Sano M. Topological defects control collective dynamics in neural progenitor cell cultures. Nature. 2017; 545(7654):327–331.

Killeen A, Bertrand T, Lee CF. Polar fluctuations lead to extensile nematic behavior in confluent tissues. Physical Review Letters. 2022; 128(7):078001.

Klain DA. The minkowski problem for polytopes. Advances in Mathematics. 2004; 185(2):270–288.

Klatt MA, Hörmann M, Mecke K. Characterization of anisotropic gaussian random fields by minkowski tensors. Journal of Statistical Mechanics: Theory and Experiment. 2022; 2022(4):043301.

Koride S, Loza AJ, Sun SX. Epithelial vertex models with active biochemical regulation of contractility can explain organized collective cell motility. APL bioengineering. 2018; 2(3).

Krommydas D, Carenza LN, Giomi L. Hydrodynamic enhancement of p-atic defect dynamics. Physical Review Letters. 2023; 130(9):098101.

Laine RF, Tosheva KL, Gustafsson N, Gray RDM, Almada P, Albrecht D, Risa GT, Hurtig F, Lindås AC, Baum B, Mercer J, Leterrier C, Pereira PM, Culley S, Henriques R. NanoJ: a high-performance open-source super-resolution microscopy toolbox. Journal of Physics D: Applied Physics. 2019; 52(16):163001.

Li X, Das A, Bi D. Mechanical heterogeneity in tissues promotes rigidity and controls cellular invasion. Physical Review Letters. 2019; 123:058101.

Li YW, Ciamarra MP. Role of cell deformability in the two-dimensional melting of biological tissues. Physical Review Materials. 2018; 2(4):045602.

Loewe B, Chiang M, Marenduzzo D, Marchetti MC. Solid-liquid transition of deformable and overlapping active particles. Physical Review Letters. 2020; 125:038003.

Maroudas-Sacks Y, Garion L, Shani-Zerbib L, Livshits A, Braun E, Keren K. Topological defects in the nematic order of actin fibres as organization centres of hydra morphogenesis. Nature Physics. 2021; 17(2):251–259.

McMullen P. Isometry covariant valuations on convex bodies. In: *Second international conference in stochastic geometry, convex bodies and empirical measures, Agrigento, Italy, September 9–14, 1996* Palermo: Circolo Matematico di Palermo; 1997.p. 259–271.

Mecke KR. Additivity, convexity, and beyond: Applications of minkowski functionals in statistical physics. In: Mecke KR, Stoyan D, editors. *Statistical Physics and Spatial Statistics* Berlin, Heidelberg: Springer Berlin Heidelberg; 2000. p. 111–184.

Melo S, Guerrero P, Moreira Soares M, Bordin JR, Carneiro F, Carneiro P, Dias MB, Carvalho J, Figueiredo J, Seruca R, Travasso RDM. The ECM and tissue architecture are major determinants of early invasion mediated by E-cadherin dysfunction. Communications Biology. 2023; 6(1):1132.

Mickel W, Kapfer SC, Schröder-Turk GE, Mecke K. Shortcomings of the bond orientational order parameters for the analysis of disordered particulate matter. The Journal of Chemical Physics. 2013; 138(4):044501.

Minkowski H. Allgemeine Lehrsätze über die convexen Polyeder. Nachrichten von der Gesellschaft der Wissenschaften zu Göttingen, Mathematisch-Physikalische Klasse. 1897; 1897:198–220.

Monfared S, Ravichandran G, Andrade J, Doostmohammadi A. Mechanical basis and topological routes to cell elimination. eLife. 2023; 12:e82435.

Moure A, Gomez H. Phase-field modeling of individual and collective cell migration. Archives of Computational Methods in Engineering. 2021; 28:311–344.

Mueller R, Yeomans JM, Doostmohammadi A. Emergence of active nematic behavior in monolayers of isotropic cells. Physical Review Letters. 2019; 122:048004.

Murray CA, Van Winkle DH. Experimental observation of two-stage melting in a classical two-dimensional screened coulomb system. Physical Review Letters. 1987 Mar; 58:1200–1203.

Nelson DR, Halperin BI. Dislocation-mediated melting in two dimensions. Physical Review B. 1979 Mar; 19:2457–2484.

Onsager L. The effects of shape on the interaction of colloidal particales. Annals of the New York Academy of Sciences. 1949; 51(4):627–659.

Pasupalak A, Yan-Wei L, Ni R, Ciamarra MP. Hexatic phase in a model of active biological tissues. Soft matter. 2020; 16(16):3914–3920.

Praetorius S, Voigt A. Collective cell behaviour – a cell-based parallelisation approach for a phase field active polar gel model. No. 49 in NIC Series, Jülich: Forschungszentrum Jülich GmbH, Zentralbibliothek; 2018.

Pylvänäinen JW, Laine RF, Saraiva BMS, Ghimire S, Follain G, Henriques R, Jacquemet G. Fast4DReg: Fast registration of 4D microscopy datasets. bioRxiv. 2022; https://www.biorxiv.org/content/early/2022/10/14/2022.08.22.504744.

Ravichandran Y, Vogg M, Kruse K, Pearce DJ, Roux A. Topology changes of the regenerating hydra define actin nematic defects as mechanical organizers of morphogenesis. bioRxiv. 2024; p. 2024–04.

Salvalaglio M, Voigt A, Wise SM. Doubly degenerate diffuse interface models of surface diffusion. Mathematical Methods in the Applied Sciences. 2021; 44:5385–5405.

Saw TB, Doostmohammadi A, Nier V, Kocgozlu L, Thampi S, Toyama Y, Marcq P, Lim CT, Yeomans JM, Ladoux B. Topological defects in epithelia govern cell death and extrusion. Nature. 2017; 544(7649):212–216.

Saye RI, Sethian JA. Analysis and applications of the voronoi implicit interface method. Journal of Computational Physics. 2012; 231(18):6051–6085.

Saye RI, Sethian JA. The voronoi implicit interface method for computing multiphase physics. Proceedings of the National Academy of Science. 2011; 108(49):19498–19503.

Schaller F, Kapfer S, Klatt M, Hug D, Last G, Mecke K, Schröder-Turk G, morphometry.org; 2024. https://morphometry.org.

Schneider R. Convex bodies: The Brunn–Minkowski theory. Encyclopedia of Mathematics and its Applications, Cambridge University Press; 2013.

Schröder-Turk GE, Mickel W, Kapfer SC, Schaller FM, Breidenbach B, Hug D, Mecke K. Minkowski tensors of anisotropic spatial structure. New Journal of Physics. 2013; 15(8):083028.

Schröder-Turk GE, Mickel W, Schröter M, Delaney GW, Saadatfar M, Senden TJ, Mecke K, Aste T. Disordered spherical bead packs are anisotropic. Europhysics Letters. 2010; 90(3):34001.

Schröder-Turk GE, Kapfer S, Breidenbach B, Beisbart C, Mecke K. Tensorial minkowski functionals and anisotropy measures for planar patterns. Journal of Microscopy. 2010; 238(1):57–74.

Sknepnek R, Djafer-Cherif I, Chuai M, Weijer C, Henkes S. Generating active T1 transitions through mechanochemical feedback. eLife. 2023; 12:e79862.

Stringer C, Wang T, Michaelos M, Pachitariu M. Cellpose: a generalist algorithm for cellular segmentation. Nature Methods. 2021; 18:100–106.

Tinevez JY, Perry N, Schindelin J, Hoopes GM, Reynolds GD, Laplantine E, Bednarek SY, Shorte SL, Eliceiri KW. TrackMate: An open and extensible platform for single-particle tracking. Methods. 2017; 115:80–90.

Tong S, Sknepnek R, Košmrlj A. Linear viscoelastic response of the vertex model with internal and external dissipation: Normal modes analysis. Physical Review Research. 2023; 5(1):013143.

Vaxman A, Campen M, Diamanti O, Panozzo D, Bommes D, Hildebrandt K, Ben-Chen M. Directional field synthesis, design, and processing. Computer Graphics Forum. 2016; 35(2):545–572.

Vey S, Voigt A. AMDiS: Adaptive multidimensional simulations. Computing and Visualization in Science. 2007; 10(1):57–67.

Virga EG. Octupolar order in two dimensions. The European Physical Journal E. 2015; 38(6).

Wang PY, Mason TG. A Brownian quasi-crystal of pre-assembled colloidal penrose tiles. Nature. 2018; 561(7721):94–99.

Wenzel D, Voigt A. Multiphase field models for collective cell migration. Physical Review E. 2021; 184:054410.

Witkowski T, Ling S, Praetorius S, Voigt A. Software concepts and numerical algorithms for a scalable adaptive parallel finite element method. Advances in Computational Mathematics. 2015; 41(6):1145–1177.

Wojciechowski KW, Frenkel D. Tetratic phase in the planar hard square system? Computational Methods in Science and Technology. 2004; 10:235–255.

Yu T, Mason TG. Heptatic liquid quasi-crystals by colloidal lithographic pre-assembly. Journal of Colloid and Interface Science. 2023; .

Zahn K, Lenke R, Maret G. Two-stage melting of paramagnetic colloidal crystals in two dimensions. Physical Review Letters. 1999; 82:2721–2724.

Appendix 1

Parameters for the computational models

Appendix 1—table 1. Values of the dimensionless parameters used in the active vertex model

Parameter	Description	Numerical Value
N	Number of cells	100
L	Simulation box size	10
T	Total simulation time	300
k_P	Perimeter elastic modulus	1.0
τ	Simulation time step	0.01
v_0	Self-propulsion strength (i.e. activity)	0.1 - 0.4
D_r	Rotation diffusion coefficient	0.05
p_0	Shape index of active cells	3.5 - 3.875

Appendix 1—table 2. Values of the dimensionless parameters used in the multiphase-field model simulations

Parameter	Description	Numerical Value
N	Number of cells	100
L	Simulation box size	100
T	Total simulation time	150
ϵ	Interface width	0.15
τ	Simulation time step	0.005
v_0	Self-propulsion strength (i.e. activity)	0.4 - 1.0
D_r	Rotation diffusion coefficient	0.01
α	Alignment parameter	0.1
Ca	Capillary number	0.05 - 0.2
In	Interaction number	0.1
a_a	Cell-cell attraction strength	1.0
a_r	Cell-cell repulsion strength	1.0
h	Mesh size	$5h \approx \epsilon$

Appendix 2

Coarse graining results obtained with the Minkowski tensor

For comparison with the literature we are considering a coarse-graining, following closely the strategy used in ***Armengol-Collado et al.*** (***2023***). We therefore regard the coarse-grained strength of p-atic order $Q_p = Q_p(\mathbf{x})$, which is the average of all shape functions $\frac{\psi_p}{\psi_0}$ (or equivalently $q_p e^{ip\vartheta_p}$) of cells whose center of mass $\mathbf{x}_c$ lies within a circle with radius R and center $\mathbf{x}$. In a formula this is:

$$Q_p(\mathbf{x}) = \frac{\sum_{j=1}^{100} q_p(C_j) e^{ip\vartheta_p(C_j)} \Theta(R - |\mathbf{x} - \mathbf{x}_c(C_j)|)}{\sum_{j=1}^{100} \Theta(R - |\mathbf{x} - \mathbf{x}_c(C_j)|)} \tag{18}$$

whereby the formula uses that our simulations contain 100 cells. C_i denotes the i–th cell and Θ denotes the Heaviside step function with $\Theta(x) = 0$ for $x > 0$ and $\Theta(x) = 0$ otherwise. As in ***Armengol-Collado et al.*** (***2023***) the position $\mathbf{x}$ is sampled over a square grid with spacing $R_C = \sqrt{\frac{A_C}{\pi}}$ with A_C the cell area. For ***Appendix 2 Figure 13*** and ***Appendix 2Figure 14*** we took the average over all grid points and all time instances. The figures show the resulting data for the active vertex model and the multiphase field model, respectively.

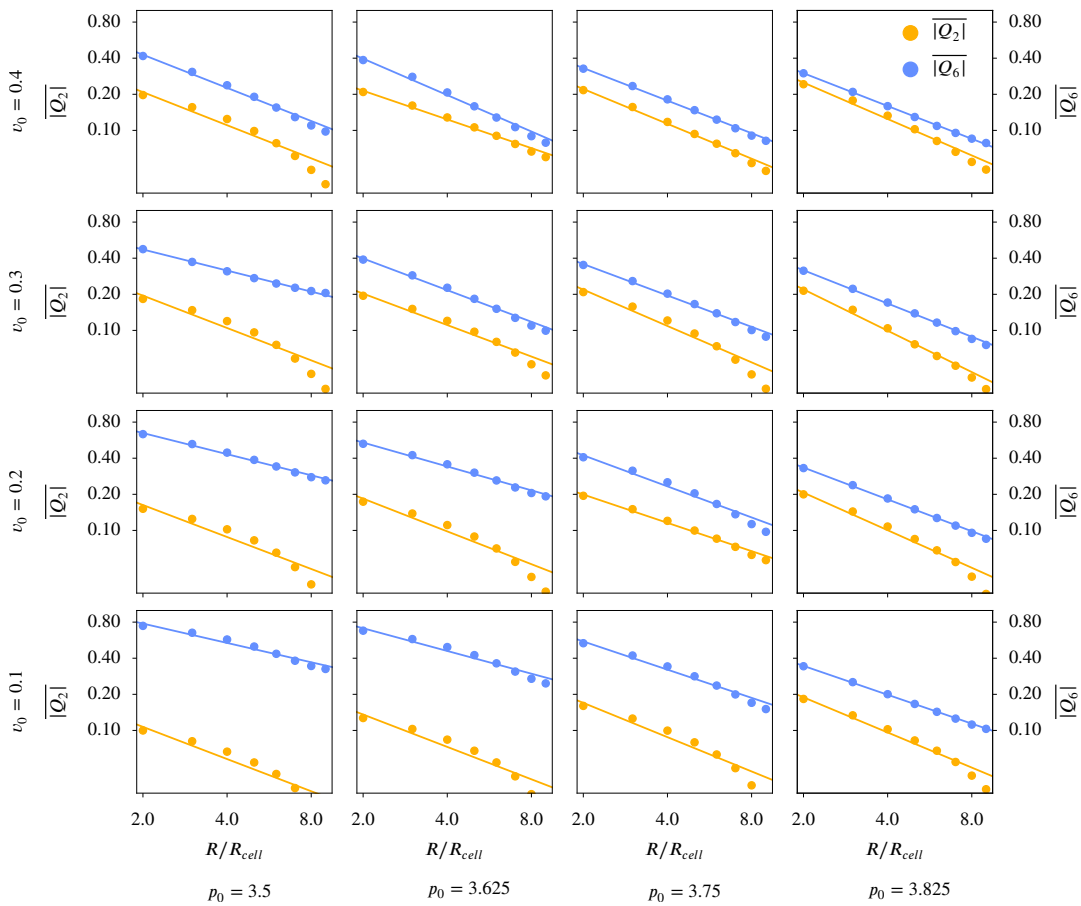

Appendix 2—figure 13. Q_6 versus Q_2 for different coarse graining radii in the active vertex model, calculated according to ***Equation 18***. A logarithmic scaling was used for both axis. q_p and ϑ_p follow from ***Equation 7***, R_C is chosen as $\sqrt{\frac{A_C}{\pi}}$.

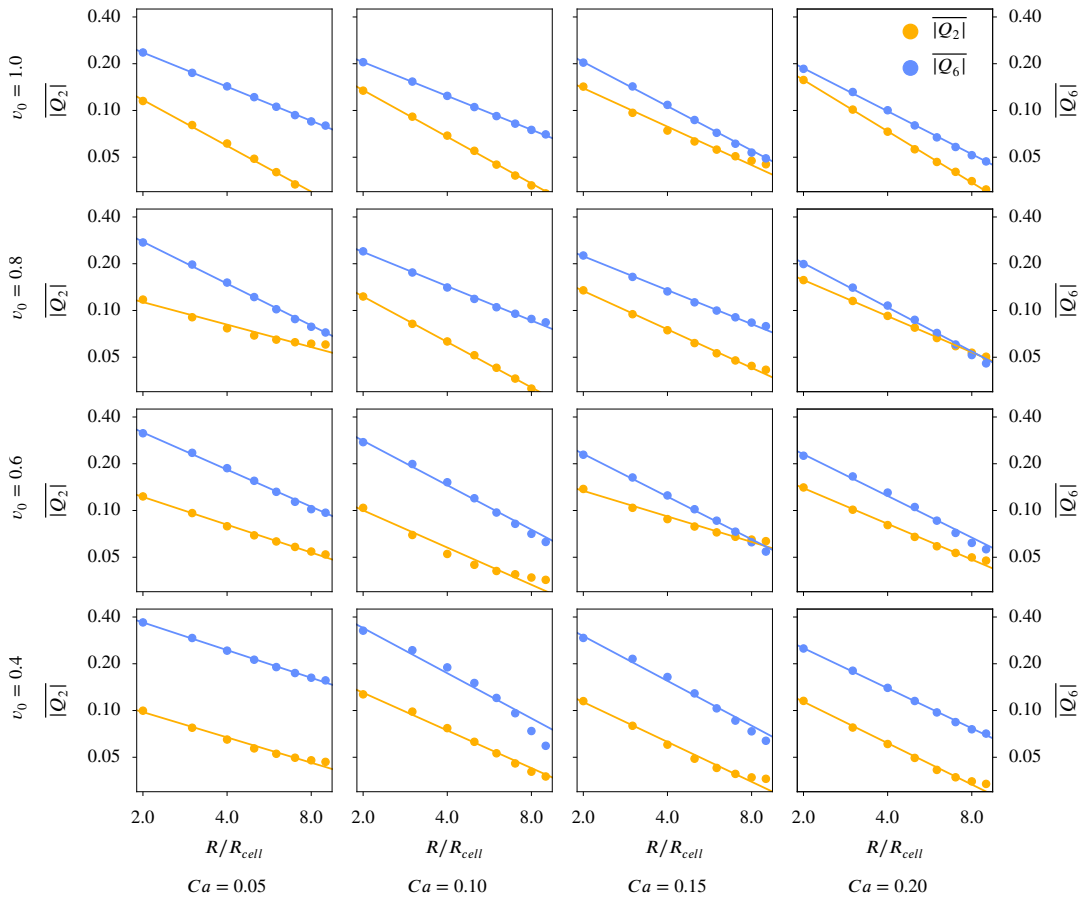

Appendix 2—figure 14. Q_6 versus Q_2 for different coarse graining radii in the multiphase field model, calculated according to ***Equation 18***. A logarithmic scaling was used for both axis. q_p and ϑ_p follow from ***Equation 7***, R_C is chosen as $\sqrt{\frac{A_C}{\pi}}$.

Appendix 3

Results using polygonal shape analysis

To visualize the similarities and differences between q_p and γ_p we show the analogue of ***Figure 4*** using the Minkowski tensors in ***Appendix 3 Figure 15*** using polygonal shape analysis. For regular polygons, both shape characterization methods behave in the same way as seen in the first row. For irregular shapes, like in the 2nd row, they already show a different behaviour. Note that the rounded shapes from ***Figure 4*** are missing in ***Appendix 3 Figure 15*** as γ_p requires a polygon.

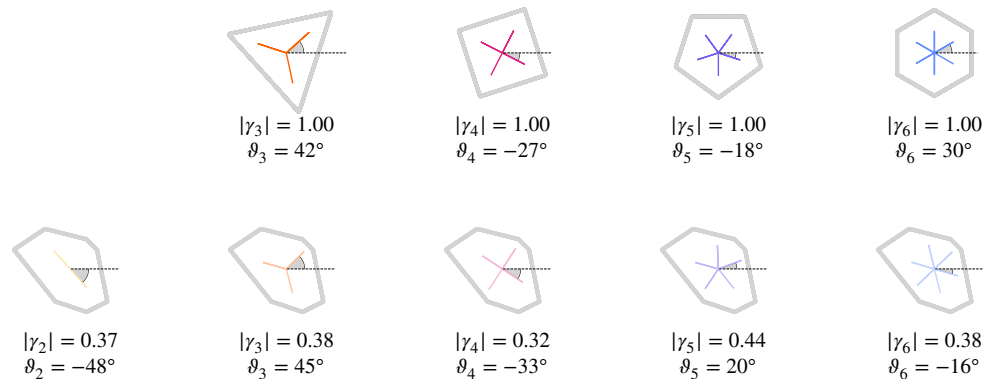

Appendix 3—figure 15. Regular and irregular shapes, adapted from ***Armengol-Collado et al.*** (***2023***), with magnitude and orientation calculated by ***Equation 8*** and ***Equation 9***. The brightness scales with the magnitude $|\gamma_p|$.

The influence of the choice of the shape characterization method is not only visible in the values for single shapes, it can also be seen in the mean and standard deviation. To illustrate this, we use γ_p to characterize the shapes from the same experimental data as in ***Figure 1*** and ***Figure 2***. The segmented data consists of smooth contours for each cell. As γ_p only works with vertex coordinates the first step is to identify these. Note that this always leads to the approximation of the cell shape with a polygon and therefore to a simplification of the shape. For finding the vertices we consider the Voronoi interface method (***Saye and Sethian, 2011***, ***2012***). Using the so obtained vertices and ***Equation 8*** and ***Equation 9*** leads to the results shown in ***Appendix 3 Figure 16*** and ***Appendix 3 Figure 17***. Compared to ***Figure 1*** and ***Figure 2***, where the Minkowski tensor was used for the same data, we see that the choice of the shape characterization method highly influences the results.

For comparison with the literature we are considering a coarse-graining, following the strategy introduced in ***Armengol-Collado et al.*** (***2023***). We therefore regard the coarse-grained shape function $\Gamma_p = \Gamma_p(\mathbf{x})$, which is the average of all shape functions γ_p of cells whose center of mass $\mathbf{x}_c$ lies within a circle with radius R and center $\mathbf{x}$. In a formula this is:

$$\Gamma_p(\mathbf{x}) = \frac{\sum_{j=1}^{100} \gamma_p(C_j)\Theta(R - |\mathbf{x} - \mathbf{x}_c(C_j)|)}{\sum_{j=1}^{100} \Theta(R - |\mathbf{x} - \mathbf{x}_c(C_j)|)} \tag{19}$$

whereby the formula uses that our simulations contain 100 cells. C_i denotes the i–th cell and Θ denotes the Heaviside step function with $\Theta(x) = 0$ for $x > 0$ and $\Theta(x) = 0$ otherwise. As in ***Armengol-Collado et al.*** (***2023***) the position $\mathbf{x}$ is sampled over a square grid with spacing $R_C = \sqrt{\frac{A_C}{\pi}}$ with A_C the cell area. For ***Appendix 3 Figure 20*** we took the average of Γ_p over all grid points and all time instances. The figure shows the resulting data for the active vertex model.

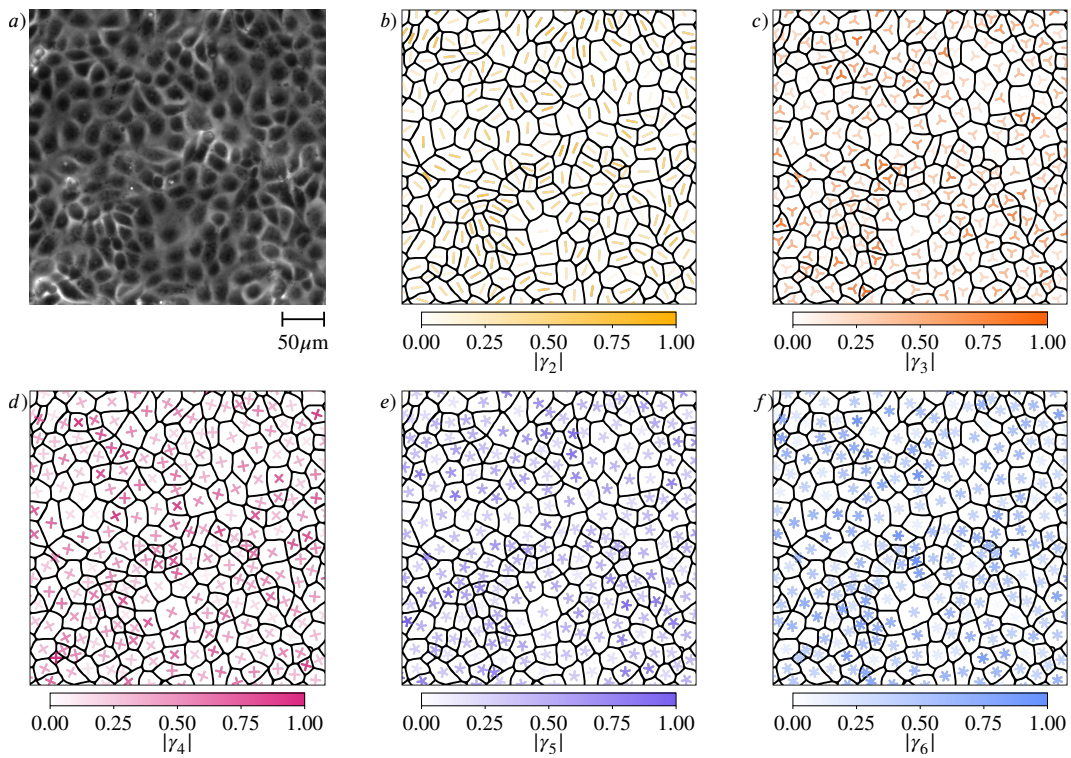

Appendix 3—figure 16. Shape classification of cells in wild-type MDCK cell monolayer. a) Raw experimental data. b) - f) Polygonal shape classification, visualized using γ_p calculated by ***Equation 8*** and ***Equation 9*** for $p = 2, 3, 4, 5, 6$, respectively. The brightness and the rotation of the p-atic director indicates the magnitude and the orientation, respectively.

a)

p	$\overline{\lvert\gamma_p\rvert}$	$\sigma(\lvert\gamma_p\rvert)$
2	0.376	0.172
3	0.338	0.181
4	0.404	0.200
5	0.403	0.184
6	0.441	0.195

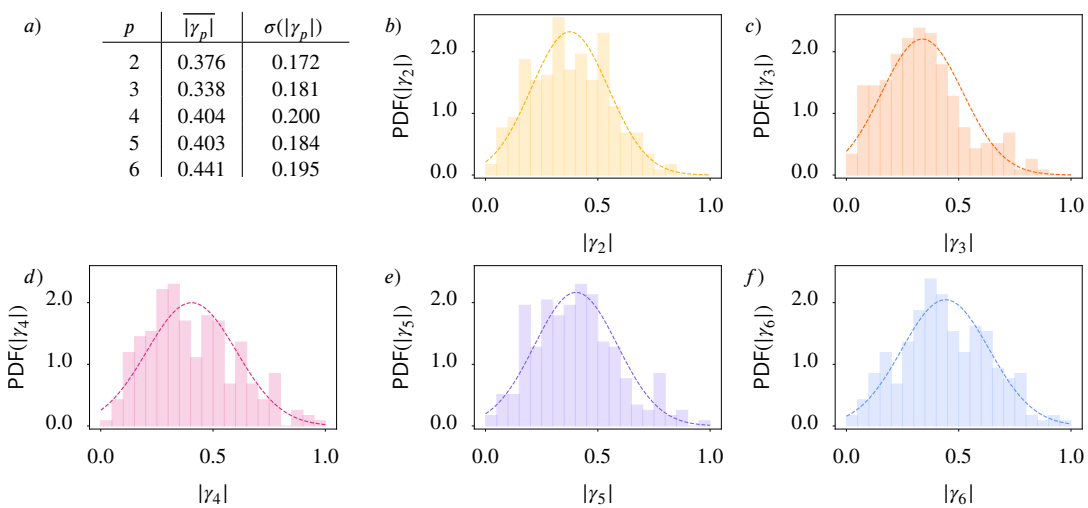

Appendix 3—figure 17. Statistical data for cell shapes identified in ***Appendix 3 Figure 16*** (. a) Mean $\overline{\lvert\gamma_p\rvert}$ and standard deviation $\sigma(\lvert\gamma_p\rvert)$ of $\lvert\gamma_p\rvert$. b) - f) Probability distribution function (PDF) of $\lvert\gamma_p\rvert$ for $p = 2, 3, 4, 5, 6$, respectively. Normal distributions with the same mean and standard deviations are added to the histograms as a guide to the eye.

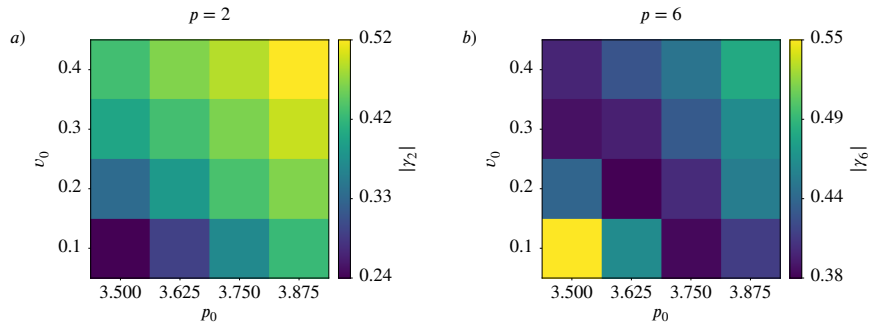

Appendix 3—figure 18. Mean value $\overline{\gamma_p}$ as function of deformability p_0 and activity v_0 for active vertex model. a) nematic order ($p = 2$), b) hexatic order ($p = 6$). While the behaviour of $|\gamma_2|$ qualitatively agrees with the behaviour of q_2, the behaviour of $|\gamma_6|$ is quite different to the one of q_6.

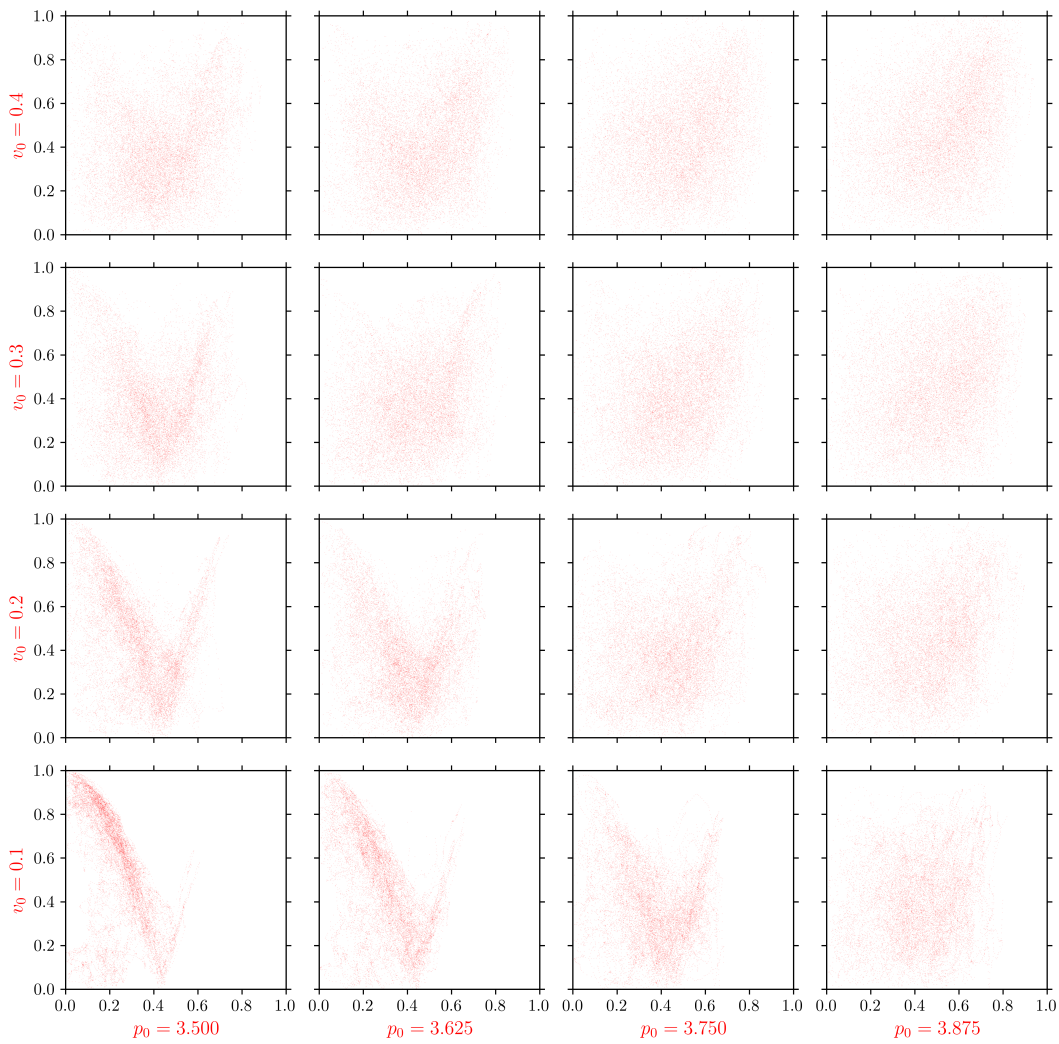

Appendix 3—figure 19. γ_6 (y-axis) versus γ_2 (x-axis) for all cells in the active vertex model. For each cell and each timestep we plot one point (γ_2, γ_6). Each panel corresponds to specific model parameters p_0 and v_0, representing deformability and activity.

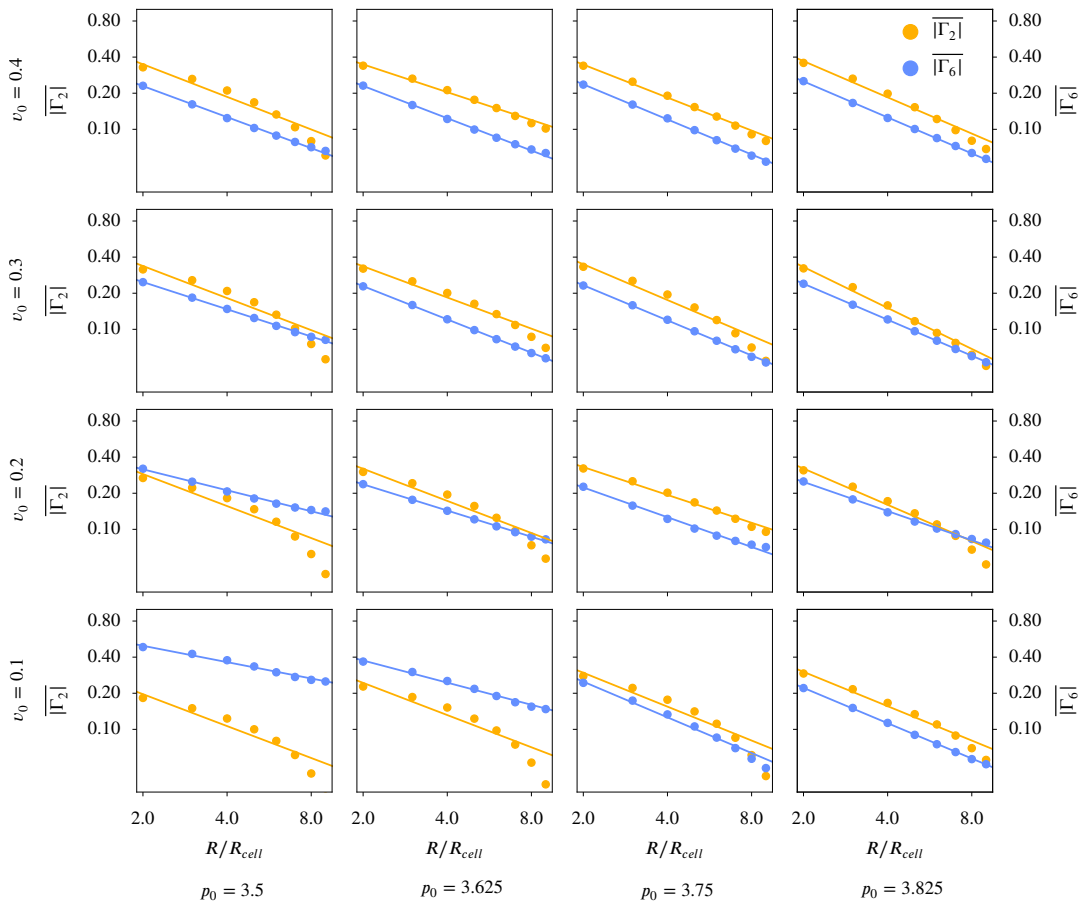

Appendix 3—figure 20. Γ_6 versus Γ_2 for different coarse graining radii in the active vertex model, calculated according to ***Equation 19***. A logarithmic scaling was used for both axis. γ_p follows from ***Equation 8***, R_C is chosen as $\sqrt{\frac{A_C}{\pi}}$.

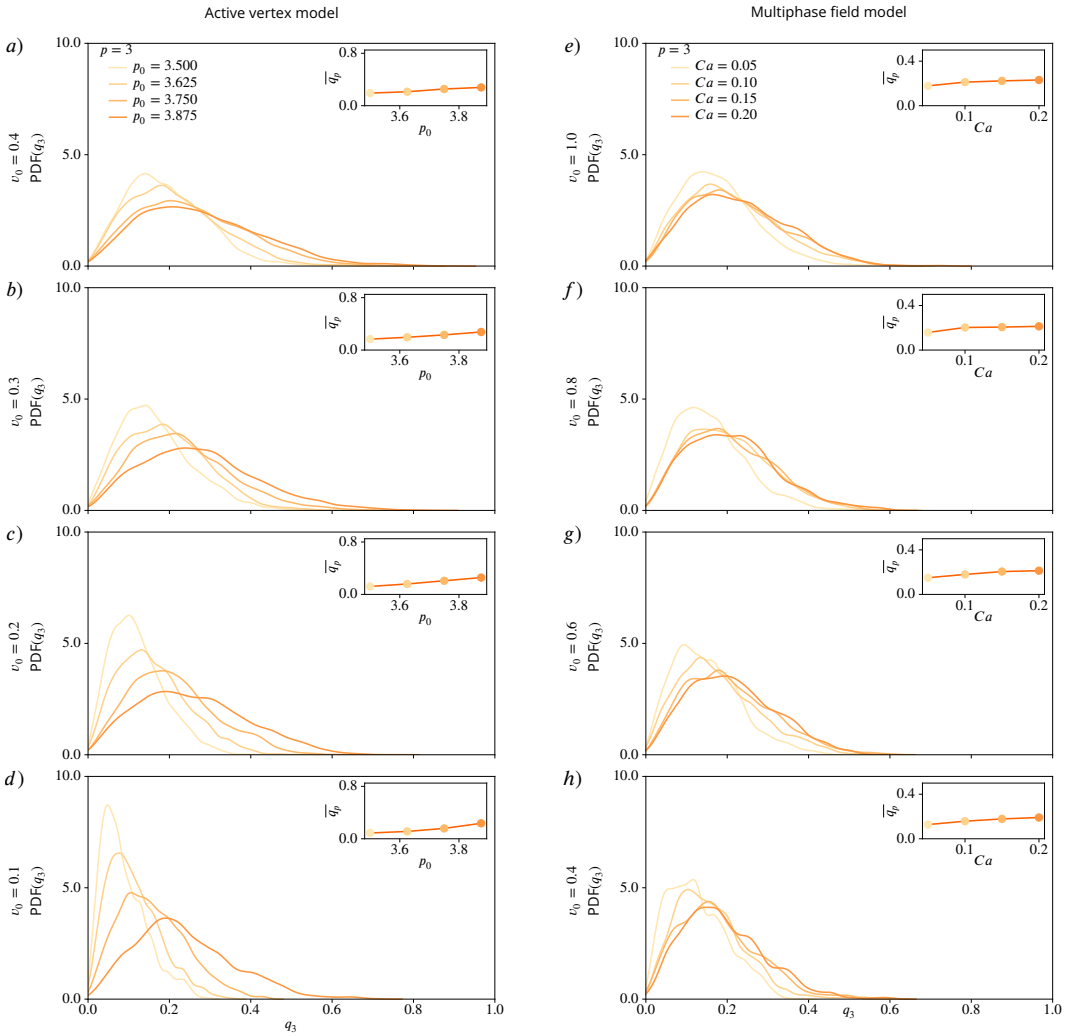

Figure 8—figure supplement 1. PDFs for q_3 using kde-plots, for varying deformability p_0 or Ca and fixed activity v_0. Inlets show mean values of q_3 as function of deformability. a) - d) active vertex model, e) - h) multiphase field model for descreasing activity.

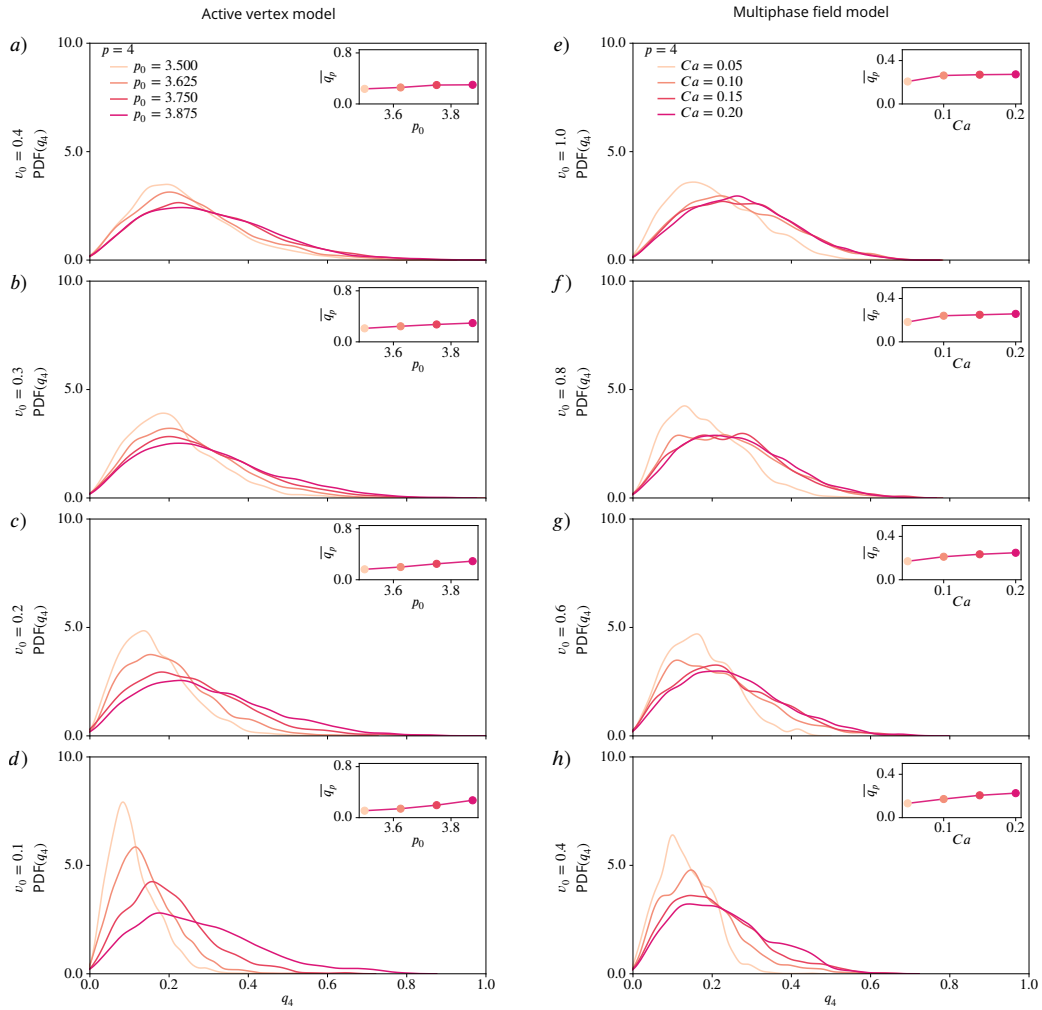

Figure 8—figure supplement 2. PDFs for q_4 using kde-plots, for varying deformability p_0 or Ca and fixed activity v_0. Inlets show mean values of q_4 as function of deformability. a) - d) active vertex model, e) - h) multiphase field model for decreasing activity.

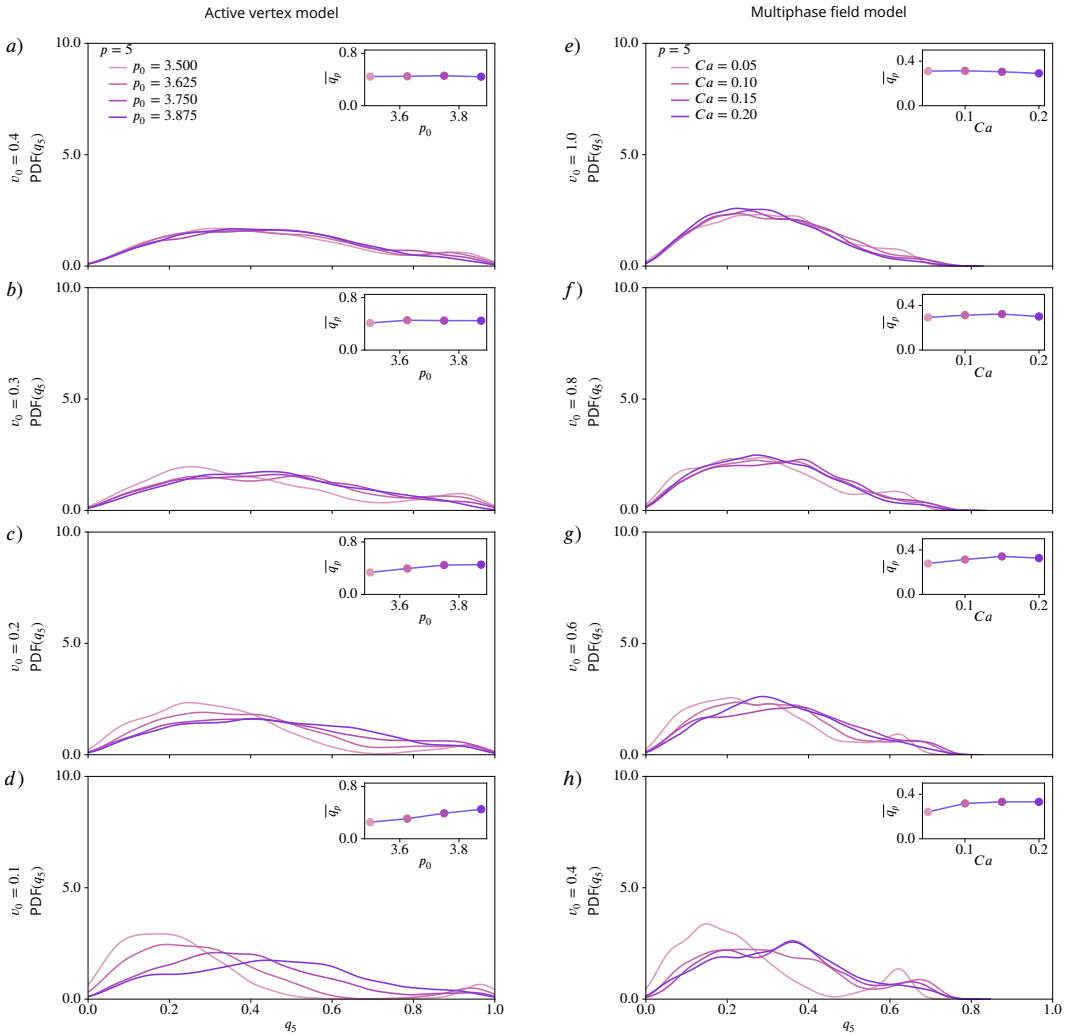

Figure 8—figure supplement 3. PDFs for q_5 using kde-plots, for varying deformability p_0 or Ca and fixed activity v_0. Inlets show mean values of q_5 as function of deformability. a) - d) active vertex model, e) - h) multiphase field model for decreasing activity.

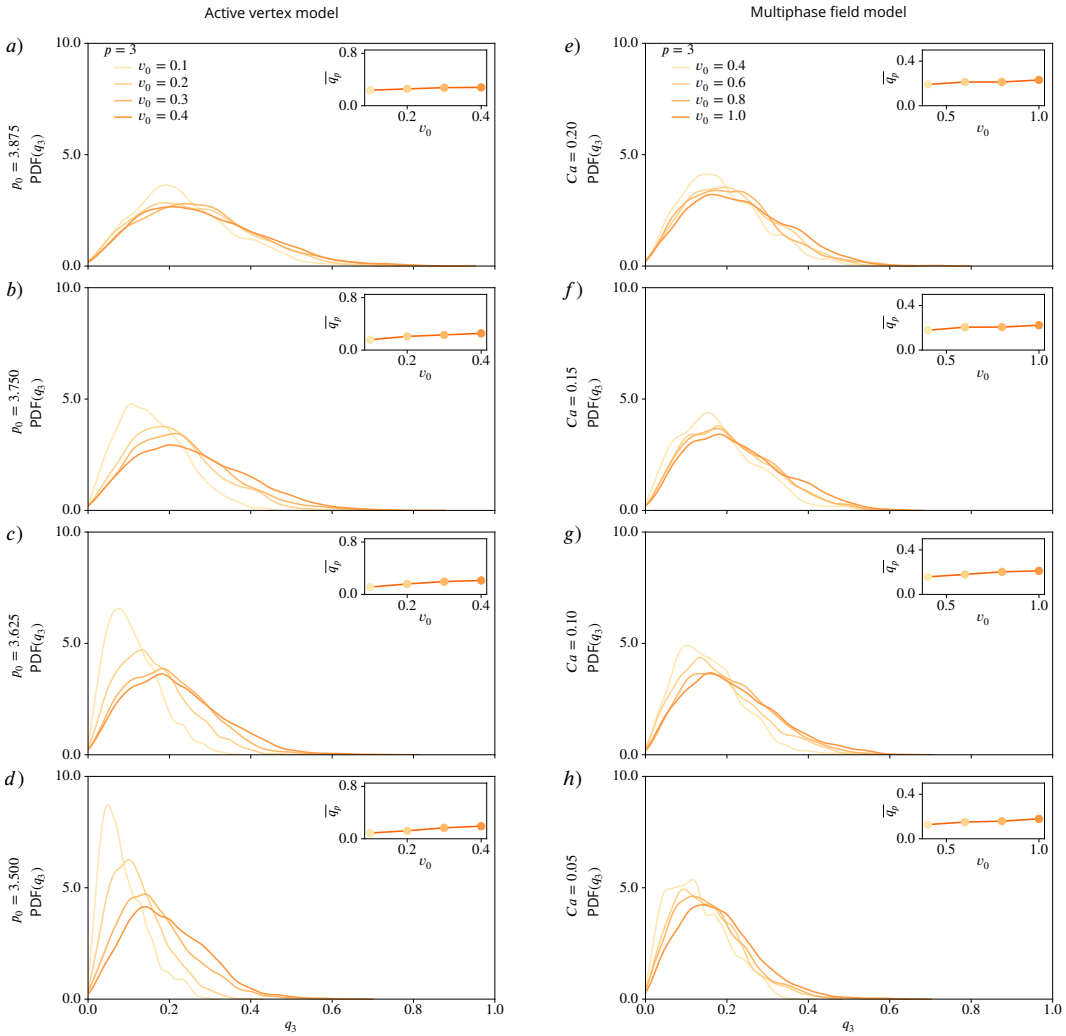

Figure 9—figure supplement 1. PDFs for q_3 using kde-plots, for varying activity v_0 and fixed deformability p_0 or Ca. Inlets show mean values of q_3 as function of activity. a) - d) active vertex model and e) - h) multiphase field model for decreasing deformability.

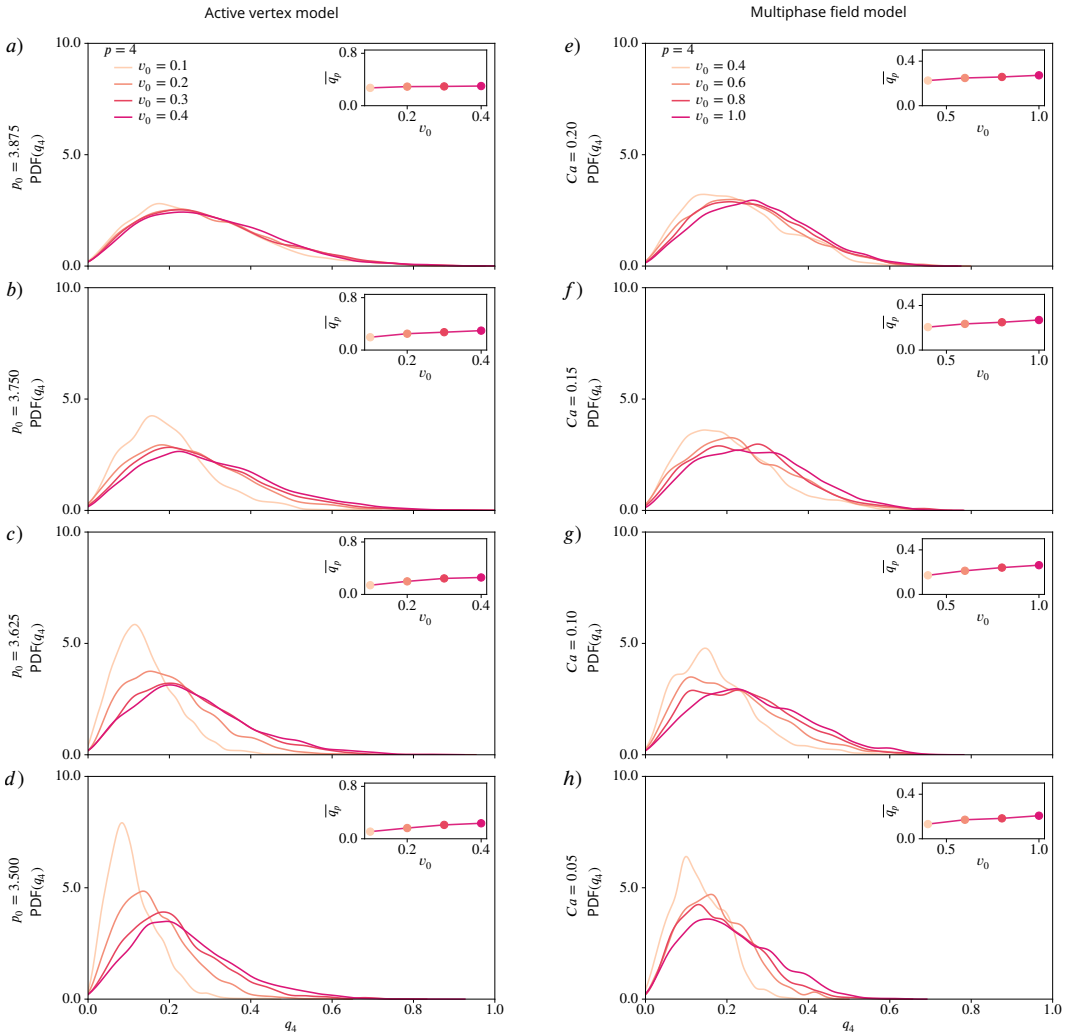

Figure 9—figure supplement 2. PDFs for q_4 using kde-plots, for varying activity v_0 and fixed deformability p_0 or Ca. Inlets show mean values of q_4 as function of activity. a) - d) active vertex model and e) - h) multiphase field model for decreasing deformability.

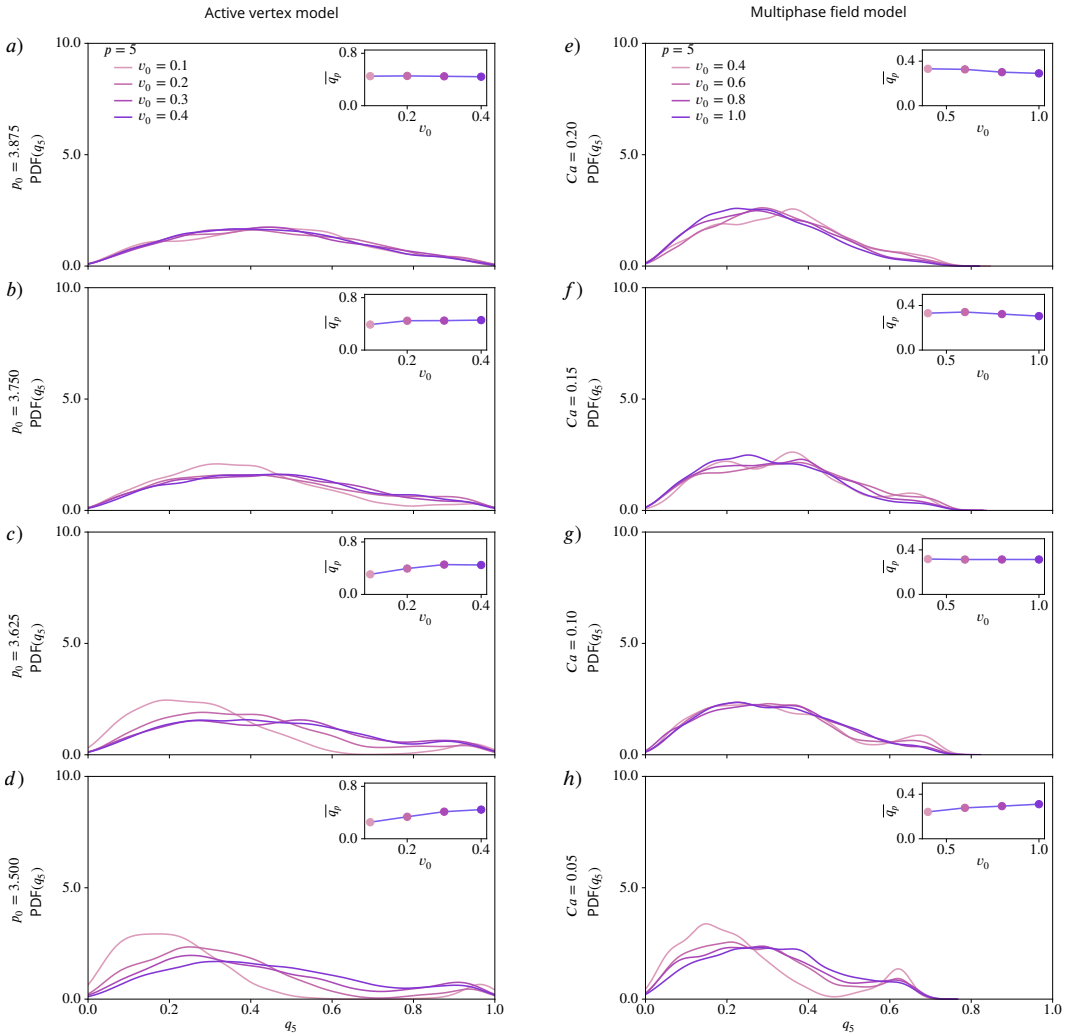

Figure 9—figure supplement 3. PDFs for q_5 using kde-plots, for varying activity v_0 and fixed deformability p_0 or Ca. Inlets show mean values of q_5 as function of activity. a) - d) active vertex model and e) - h) multiphase field model for decreasing deformability.

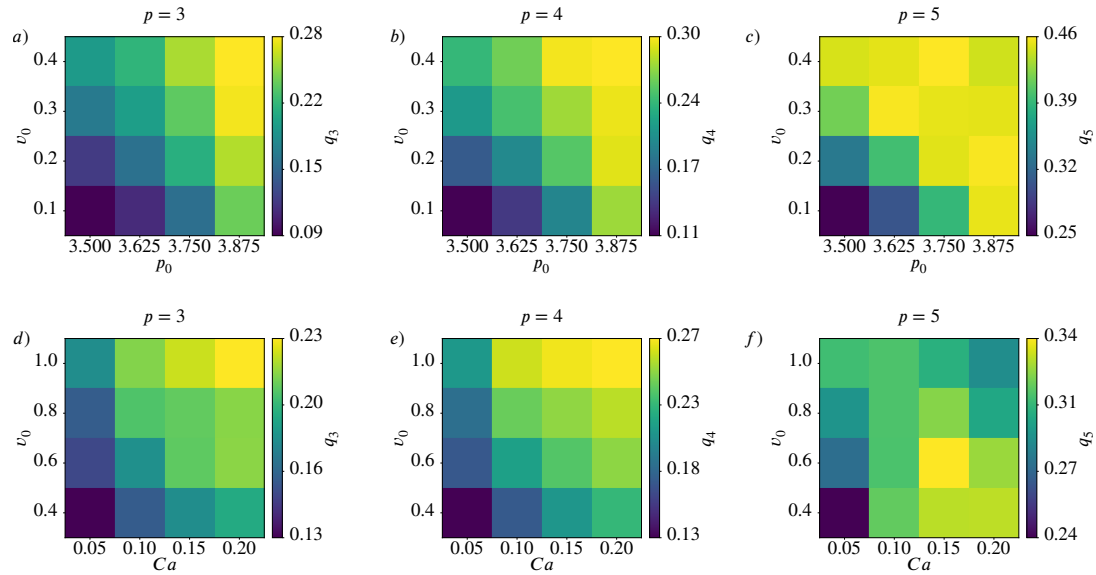

Figure 10—figure supplement 1. Mean value $\overline{q_p}$ for $p = 3$ (left), $p = 4$ (middle) and $p = 5$ (right) as function of deformability p_0 or Ca and activity v_0 for active vertex model (a) - c)) and multiphase field model (d) - f)).